# NOTICE

# AVIS

The quality of this microform is heavily dependent upon the quality of the original thesis submitted for microfilming. Every effort has been made to ensure the highest quality of reproduction possible.

If pages are missing, contact the university which granted the degree.

Some pages may have indistinct print especially if the original pages were typed with a poor typewriter ribbon or if the university sent us an inferior photocopy.

Previously copyrighted materials (journal articles, published tests, etc.) are not filmed.

Reproduction in full or in part of this microform is governed by the Canadian Copyright Act, R.S.C. 1970, c. C-30.

La qualité de cette microforme dépend grandement de la qualité de la thèse soumise au microfilmage. Nous avons tout fait pour assurer une qualité supérieure de reproduction.

S'il manque des pages, veuillez communiquer avec l'université qui a conféré le grade.

La qualité d'impression de certaines pages peut laisser à désirer, surtout si les pages originales ont été dactylographiées à l'aide d'un ruban usé ou si l'université nous a fait parvenir une photocopie de qualité inférieure.

Les documents qui font déjà l'objet d'un droit d'auteur (articles de revue, tests publiés, etc.) ne sont pas microfilmés.

La reproduction, même partielle, de cette microforme est soumise à la Loi canadienne sur le droit d'auteur, SRC 1970, c. C-30.

Canada

Finite Volume Solutions of the Euler Equations on Cartesian grids

Rajnish Chandrasekhar

A Thesis

in

The Department

of

Mechanical Engineering

Presented in Partial Fulfillment of the Requirements
for the Degree of Master of Engineering at
Concordia University
Montréal, Québec, Canada

March 1988

# ABSTRACT

### Finite Volume Solutions of the Euler Equations on Cartesian Grids

### Rajnish Chandrasekhar

This thesis deals with the development of a code for the numerical calculation of two-dimensional inviscid flows over airfoils, by using the primitive variables form of the unsteady Euler equations. A Cartesian grid is used for the spatial discretization of the flow domain into finite volumes and the solution is obtained by marching in time using Jameson's fourth order Runge-Kutta time-stepping procedure. The results obtained cover subsonic and transonic flows for both lifting and non-lifting test cases on a NACA 0012 airfoil and are in reasonable agreement with other calculations. Finally, an extension to a multi-element airfoil has been carried out.

# ACKNOWLEDGEMENTS

# TABLE OF CONTENTS

| Chapter | Title | Page Number |
|---|---|---|

# NOMENCLATURE

| | | |
|---|---|---|
| $\rho$ | = | fluid density |
| $u$ | = | fluid velocity in horizontal direction |
| $v$ | = | fluid velocity in vertical direction |
| $p$ | = | fluid pressure |
| $E$ | = | total energy per unit mass of fluid |
| $H$ | = | total enthalpy per unit mass of fluid |
| $\gamma$ | = | ratio of specific heat capacities |
| $x, y$ | = | coordinates of physical domain |
| $\xi, \eta$ | = | coordinates of computational domain |
| $i, j$ | = | location of a finite volume cell |
| $A_{i,j}$ | = | area of a finite volume cell |
| $\Delta t$ | = | time step |
| $\lambda$ | = | Courant Number |
| $\lambda'$ | = | eigenvalues of Euler equations |
| $c$ | = | speed of sound $= (\gamma \cdot p / \rho)^{1/2}$ |
| $D$ | = | artificial dissipation term |
| $F_{i,j}$ | = | flux balance over a finite volume cell |
| $\infty$ | = | freestream conditions |
| $x/c, y/c$ | = | coordinates of airfoil, normalized with respect to chord length |
| $C_p$ | = | pressure coefficient |

# CHAPTER 1

# INTRODUCTION

## § 1.1 Background & Literature Review :

For the range of flight speeds of most aircraft, the airflow outside the boundary layer on the aircraft surface can be considered inviscid. Either the potential equation or the Euler equations can be used to represent this outer inviscid flow. The use of the potential equation is based on the assumption that the flow is irrotational and isentropic. This model serves adequately for flows with weak shocks. However, Steinhoff and Jameson (Ref. 1) showed that multiple solutions of this equation could be obtained for a symmetric airfoil, at a fixed transonic Mach Number and in a small range of angles of attack. Subsequently, a comparative study of this non-uniqueness of the potential equation was carried out by Salas et al (Ref. 2). In addition to these problems encountered in external flows, a unique potential solution may not exist for choked nozzle flows with a prescribed back pressure. This is because the location of the shock is determined by the entropy rise, which is ignored in the potential model.

Furthermore, the entropy gradient across a shock is proportional to the third power of the shock strength $M^2 - 1$ where M is the local upstream Mach Number at the shock. Therefore, when this Mach Number reaches 1.3 or higher, the corresponding entropy rise becomes significant and leads to a shock wave which appears further downstream in the potential model as compared to the Euler one. Hence, a closer approximation to the Euler equations can be achieved by a non-isentropic or 'modified' potential formulation, as shown by Hafez and Lovell (Ref. 3) and Habashi et al (Ref. 4). The Rankine-Hugoniot equations give the the entropy rise across the shock, which is used to calculate the total pressure. This model succeeds in overcoming the non-uniqueness problem of the potential equation. However, it does not account for the resulting vorticity production across the shock, given by Crocco's equation,

1

$$\vec{V} \times \vec{\omega} = \nabla H_0 - T \nabla S$$

where $\vec{V}$ = velocity vector ; $\vec{\omega}$ = vorticity vector = curl of $\vec{V}$

$S$ = entropy ; $H_0$ = total enthalpy

The other alternative is a stream function formulation which can account for both the entropy variation and the corresponding vorticity. Studies on this model have been done by Hafez and Lovell (Ref. 5), Habashi' and Hafez (Ref. 6), who have shown turbomachine applications and by Atkins and Hassan (Ref. 7), whose formulation does not require explicit evaluation of the vorticity.

However, the Euler model is the approximation to the Navier-Stokes equations in the limit of infinite Reynold's Number and hence serves as a convenient foundation for testing various solution algorithms. Among the earliest studies on this formulation was done by Magnus and Yoshihara (Ref. 8), who solved the unsteady Euler equations explicitly, by a Lax-Wendroff time-marching technique. The drawback of this explicit model was the long execution time required for reaching the steady state. This led to the development of implicit methods, notably that of Beam and Warming (Ref. 9), whose advantage lies in the unrestricted stability limit. Subsequent improvements in explicit methods were made by Jameson et al (Ref. 10), who used a fourth-order Runge-Kutta scheme in order to obtain a larger Courant Number than most other popularly used schemes like the Lax-Wendroff and MacCormack schemes, which are second order in time. )

Alternatively, the steady Euler equations can be solved by relaxation procedures, as shown by Dick (Ref. 11) and Johnson (Ref. 12). Dick's procedure consisted of three steps, of which the first two were a predictor-corrector set of the MacCormack type and the relaxation was carried out in the third step. Johnson showed that the first-order Euler equations could be embedded in a second-order system, which he refers to as the surrogate equation technique. Relaxation procedures which have been developed for

2

other second-order equations such as the full potential equation can be then used for solving this surrogate system.

Furthermore, the spatial discretization of the convective terms in the Euler equations can affect the stability of the solution. Since the Euler equations have both positive and negative eigenvalues, the natural choice for a neutrally stable discretization is a central differencing scheme. The convective terms of the Euler equations discretized in this manner, have complex eigenvalues. Carey (Ref. 13) studied plots of these eigenvalues (Gershgorin circles) in the complex plane, which reveal that for a purely inviscid system, the intercept on the imaginary axis is double-valued in sign. This leads to odd-even decoupling and the 'wiggles' associated with central differences. The odd and even numbered grid points give different solution families. In order to couple the odd and even points, artificial dissipation terms are necessary. Addition of these dissipation terms shifts the eigenvalue circles to the left of the real axis, thus preventing bifurcation of the imaginary part. These artificial terms must not affect the second order accuracy of the finite volume scheme and hence fourth order dissipation is preferred to the simpler second order type, for subsonic flows. Since transonic flow consists of local supersonic pockets in an overall subsonic flow, this dissipation can be adapted to the flow, switching between fourth order and second order terms.

Alternate methods of maintaining the stability of the solution scheme include the split-flux technique, as shown by Steger and Warming (Ref. 14). They separate the fluxes into positive and negative eigenvalues and use upwind and downwind differencing, respectively. This shock-capturing method can be used either for explicit or implicit algorithms and does not need addition of an artificial viscosity.

Having justified the choice of the particular solution scheme, the body boundary conditions must be examined. Since these conditions have to be satisfied accurately, the spatial discretization must be achieved through a grid that is preferably body-fitted. This

3

is achieved through transformations that connect the grid points from the computational domain to the physical domain. Commonly used mappings include algebraic methods and methods based on the solution of partial differential equations. In the latter case, an elliptic equation can be used to determine the internal grid point spacing, after the points on the outer boundaries have been specified. Alternatively, a hyperbolic equation is solved by marching towards the outer boundary after specifying the grid points on the airfoil surface. In order to eliminate cross-derivative terms in the transformation metrics, it is desirable to have an orthogonal grid. This can be achieved through the use of conformal mappings (Ref. 15). The coordinate system resulting from a conformal mapping can have singularities at corners like trailing edges. If a grid has to be constructed for a multiply-connected region, for example an airfoil with a flap or a wing-pylon configuration, then special treatment of these singularities is required and several techniques are used by different authors to patch the various sub-regions together. Therefore, interpolating functions must be used at the neighbouring corners leading to discontinuous transformation metrics. Transfinite interpolation is a reasonable solution to this problem and uses interpolating functions from finite element methodology to obtain local continuity of transformation metrics. Also, in order to use finite volume methods, it is necessary to have grids with minimum skewness. Hence, Wedan and South (Ref. 16) avoided this mapping problem by applying a simple Cartesian grid to internal flow and single airfoil problems and (Ref. 17) shows the application of Cartesian grids to multi-element airfoils.

The use of finite volume methods to discretize the flow domain makes it possible to satisfy the body boundary conditions accurately, irrespective of the shape of the boundary. This is similar to the advantage offered by finite element methods, where the sides of some elements approximate the body surface. However, finite volume methods have the advantage of simplicity of calculations of finite difference methods.

4

## § 1.2 Problem Statement and Scope :

In the present work, the unsteady, two-dimensional Euler equations are solved for in primitive variable form. A simple Cartesian grid is used for the spatial discretization of the flow into finite volumes. The equations are written in divergence form to ensure conservation of fluxes across cell interfaces. The finite volume formulation ensures conservation of mass, momentum and energy within a cell. The solution is marched in time using a fourth order Runge-Kutta time-stepping procedure and stability is maintained through addition of artificial dissipation terms.

Given this background, the objectives of this thesis can be stated as follows :

(1) To develop an Euler code using finite volume discretization of the flow-field, on simple Cartesian grids.

(2) To show that this code is capable of producing solutions in agreement with those obtained using body-fitted grids - for both lifting and non-lifting test cases on a NACA 0012 airfoil.

(3) To demonstrate that this code is also capable of solving flow problems involving multi-element airfoils.

## § 1.3 Approach and Presentation :

The core of the thesis is Chapter 2. Each article of this analysis chapter begins with a review of contemporary numerical methods for the solution of the Euler equations followed by a justification of the particular procedure being followed in the present work. Subsequently, the derived expressions are validated by running the resulting code for a variety of applications. The results are presented and discussed in Chapter 3, with reference to Figs. 6 to 15. In summary, the main engineering contribution of this Master's thesis is that an Euler code has been developed from first principles, using contemporary numerical techniques.

5

# CHAPTER 2

# ANALYSIS

Each article contains a review of several numerical methods for the solution of the Euler equations of fluid dynamics. This is followed by derivations of the particular expressions used finally in the computer code.

## § 2.1 Governing Equations :

The Navier-Stokes equations give a complete description of the fluid flow. But for flows over airfoils at high Reynolds' Numbers, the viscous effects can be ignored. This leads to the Euler equations. The Euler code solves four equations for the conservation of mass, x - and y - momentum and energy. These are two-dimensional equations and are written in conservation form as,

$$\frac{\partial w}{\partial t} + \frac{\partial f}{\partial x} + \frac{\partial g}{\partial y} = 0 \qquad (1)$$

where,

$$w = \lfloor \rho, \rho u, \rho v, \rho E \rfloor$$

$$f = \lfloor \rho u, \rho u^2 + p, \rho uv, \rho uH \rfloor$$

$$g = \lfloor \rho v, \rho uv, \rho v^2 + p, \rho vH \rfloor \qquad (2)$$

and the quantities $\rho, u, v, p$ and $E$ are termed as primitive variables.

For an ideal gas, the total enthalpy per unit mass is expressed as,

$$H = \frac{\gamma . p}{(\gamma - 1) \rho} + \frac{1}{2}(u^2 + v^2) \qquad (3a)$$

where the equation of state, at a temperature $T$ and gas constant $R$ gives,

$$p = \rho R T \qquad (3b)$$

6

The integral form of the Euler equation system (1) is obtained from the divergence theorem as,

$$\frac{\partial}{\partial t} \iint_S w \, dx \, dy \quad + \quad \int_{dS} (f \, dy - g \, dx) \quad = \quad 0 \qquad (4)$$

over a domain S (which is a finite volume cell) with a boundary dS.

## § 2.2   Grid Generation :

It is well known that there are basically two types of grid generation techniques, namely algebraic methods and methods based on the solution of partial differential equations. Various transformations can be used to connect the grid points from the computational $\zeta$ - plane, to the physical z - plane. In order to eliminate cross-derivative terms in the transformation metrics, it is desirable to have an orthogonal grid. This can be achieved through conformal mappings (Ref. 15). The Joukowski and Karman-Trefftz airfoils are examples of boundaries treated like this. The conformal mappings may be expressed as a series approximation for z, and it is necessary to determine the coefficients of these series. But the resulting coordinate system can have singularities at finite distances from the boundary - so, only a portion of the coordinate system can be used. This poses a problem for multiply - connected regions, like an airfoil with a flap, or a wing - pylon configuration, etc. Other problems like patching techniques have been discussed earlier in the introductory chapter. Because of all these problems with body - fitted grids, Wedan and South (Ref. 16) pioneered the application of Cartesian grids generated by simple algebraic transformations.

The rectangular or H - grid system used in this thesis is based on the formulation proposed in Refs. (16), (18) and (19). The grid generation procedure begins with setting the left, right, upper and lower boundaries of the computational $(\xi, \eta)$ plane as follows : Horizontal $(\xi)$ and vertical $(\eta)$ ranges are given as,

7

$$-\frac{\pi}{2} + \varepsilon \leq \xi, \eta \leq \frac{\pi}{2} - \varepsilon$$

where $\varepsilon$ is a small number. The next step is to compute the finite volume cell side lengths. For example, for a (N x M) grid used for an airfoil, the cell side lengths would be,

$$\Delta \xi = \frac{\text{left boundary} - \text{right boundary}}{N - 4}$$

$$\Delta \eta = \frac{\text{upper boundary} - \text{lower boundary}}{M - 4}$$

This is because the grid boundaries are chosen as,

$$3 \leq i \leq N - 2, \quad \text{for all } x_i \text{ and } \xi_i$$

$$3 \leq j \leq M - 2, \quad \text{for all } y_j \text{ and } \eta_j$$

so that a margin of two cells can be set at all far-field boundaries for use in the dissipation calculations, as demonstrated later. A spline fit of the airfoil coordinates is made, using a package developed in Refs. (18) and (19) and the intersections of the body contour and the grid lines is determined, giving the left and right boundaries - for the $\xi$ coordinates and the upper and lower boundaries - for the $\eta$ coordinates. The cell areas can then be computed according to a general expression given as,

$$\text{Area} = \frac{1}{4} \cdot (S_x \cdot S_y + S_x \cdot D_y + S_y \cdot D_x + D_x \cdot D_y) \qquad (5)$$

where with reference to Fig. 1,

$$S_x = S_2 + S_4$$

$$S_y = S_1 + S_3$$

$$D_x = |S_4 - S_2|$$

$$D_y = |S_3 - S_1|$$

8

Consider the boundary cell as in Fig. 2. It is readily seen that its area is,

$$S_4 . S_3 \;\; \longrightarrow \;\; \frac{1}{2}(S_4 + S_2) . (S_1 - S_3)$$

The area of a full cell $= \Delta\xi . \Delta\eta$ is similarly equal to,

$$S_1 . S_4 \;\; = \;\; S_2 . S_3 \;\; = \;\; S_2 . S_1 \;\; = \;\; S_4 . S_3$$

These two cases are covered by equation (5), where the D terms are non-zero only for the boundary cells on the airfoil surface. Thus equation (5) is valid for any cell provided that the lengths of cell sides contained completely within the body are set to zero.

The spline fit of the airfoil may produce cells with very small areas as compared to neighbouring cells, leading to large variations in time steps. This is because the time steps depend on the side lengths of the cells, as demonstrated later. Since this can destabilize the solution, this problem can be overcome by comparing the areas of boundary cells, with the areas of cells immediately above or below them. As an example consider the upper surface (see Fig. 3). If the boundary cell area (see Fig. 2) is less than or equal to 50 % of the area $\Delta\xi . \Delta\eta$ of a full cell, it is added to the cell immediately above. Therefore, as shown in Fig. 3, the cell $(i , j-1)$ is added to the cell $(i, j)$. The boundary of the new augmented cell is shown by the dashed line (see Fig. 3).

## § 2.3 . Grid Transformation :

As introduced earlier, the grid generation is an algebraic method. For such problems it is simply a matter of choosing a stretching and clustering function for the transformation. Among papers on Cartesian grids, the following stretching functions are noteworthy. Wedan and South (Ref. 16) use a stretching function for their grid as,

$$x_{i+1} \;\; = \;\; x_i + (\Delta x_i)^\alpha$$

where, $\Delta x_i = x_i - x_{i-1}$ and $\alpha = 1.1$.

Clarke et al (Ref. 17) use a geometric progression for the stretching in their Cartesian grid, of the type,

9

$$x_{i+1} = x_i + (x_i - x_{i-1}) \cdot \beta, \text{ where } \beta = 1.25 .$$

Consider simple trigonometric functions like $\sin x$ and $\tan x$ which are odd functions. As is seen from Fig. 4, for the region upstream of the airfoil, the coordinates $x$ and $\xi$ are negative. Similarly, for the region downstream, $x$ and $\xi > 0$. The uniform $(\xi, \eta)$ grid in the computational plane is transformed into the $(x, y)$ grid in the physical plane, according to the transformation,

$$x = A \cdot \tan \xi \cdot e^{-B\xi}$$

$$y = D \cdot \tan \eta \qquad\qquad (6a)$$

where the constants $A$, $B$ and $D$ define the clustering of the mesh points and vary typically between unity and zero, with increased clustering. For general airfoils, typical values of these constants are,

$$A = 0.8, \ B = 0.6, \ D = 0.2.$$

This gives clustering in the leading and trailing edge regions and stretching in the far-field regions (see Fig. 4), due to the exponential term in equation (6). For transonic flows, it is necessary to stretch the far-field boundaries very far away (about 16 chords away from the airfoil), in order to obtain convergence. This is done using a value for the constant $A = 8.0$, only in the region away from the airfoil. For subsonic lifting flows, only in the leading edge region, $A = 0.6$.

From equation (6), it is easy to analytically obtain the transformation metrics as;

$$\frac{\partial \xi}{\partial x} = [A \cdot e^{-B\xi} \{ \tan \xi \, (-B\xi) + \sec^2 \xi \}]^{-1},$$

$$\frac{\partial \eta}{\partial y} = \cos^2 \eta / D \qquad\qquad (6b)$$

This is a simple method of controlling the local clustering of the grid in a one-dimensional sense, where the stretching is inversely proportional to the constant $A$.

Here it is interesting to note that there are no problems associated with truncation errors arising from a numerical evaluation of the transformation metrics.

Thus the main advantage in using algebraic mappings is that they are easy to use and the metrics of the transformation can be analytically computed. They can also be applied to three - dimensional problems in a straightforward way, with the same function used for the three directions (Ref. 20). After transforming the $(\xi, \eta)$ plane to the $(x, y)$ plane, the airfoil is shifted to the left of the origin by 0.5, giving the location of the leading edge at $x = -0.5$ and that of the trailing edge at $x = +0.5$.

## § 2.4  Finite Volume Discretization :

Upon applying equation (4) to each cell $(i, j)$ in the two - dimensional grid, the finite volume expressions are obtained in a mathematical form.

Therefore, with reference to Fig. 1, the continuity equation can be written as,

$$\frac{\partial}{\partial t} (\rho A)_{i,j} + \sum_{k=1}^{4} (\rho_k Q_k)_{i,j} = 0 \tag{7}$$

where,

$$k = \text{side } S_k \text{ of the cell } (i, j)$$

$$A = \text{Area of cell } (i, j)$$

$$Q_k = \Delta y_k u_k - \Delta x_k v_k = \text{net velocity flux}$$

$$\Delta y_k = S_3 - S_1 \quad , \quad \Delta x_k = S_4 - S_2 \tag{8}$$

It is to be noted that for cells that are not on or inside the airfoil, the terms $\Delta y_k$ and $\Delta x_k$ are equal to zero.

Similarly, the x - momentum equation is obtained as,

11

$$\frac{\partial}{\partial t}(\rho u A)_{i,j} + \sum_{k=1}^{4}(\rho_k u_k Q_k + \Delta y_k p_k)_{i,j} = 0. \qquad (9)$$

In equation (9), the term $\Delta p_k$ denotes the body pressure, which is non-zero if and only if $\Delta y_k$ is non-zero. The finite volume representations of the y-momentum and the energy equations can be similarly obtained.

In order to obtain a form of the finite volume representation that is computationally convenient, equation (1) can be written as,

$$\frac{\partial w}{\partial t} + \frac{\partial \xi}{\partial x} \cdot \frac{\Delta f}{\Delta \xi} + \frac{\partial \eta}{\partial y} \cdot \frac{\Delta g}{\Delta \eta} = 0 \qquad (10)$$

where terms like $\Delta f, \Delta g$, etc. are taken to be the central difference versions of the partial derivative terms. This is because the finite volume equation (4) reduces to a central difference scheme on a Cartesian grid.

It is seen that in equation (10), a transformed version of the Euler equations has been easily obtained which allows a movement from the physical plane to the computational plane and vice - versa. Multiplying equation (10) by the product $\Delta \xi \cdot \Delta \eta$, equation (11) is obtained as,

$$\frac{\partial}{\partial t}(w.\Delta \xi.\Delta \eta) + \frac{\partial \xi}{\partial x}.(\Delta f.\Delta \eta) + \frac{\partial \eta}{\partial y}.(\Delta g.\Delta \xi) = 0 \qquad (11)$$

Equation (11) has all the features of equation (4), namely the cell area $(\Delta \xi.\Delta \eta)$ in the unsteady term and the flux balances $(\Delta f.\Delta \eta)$ and $(\Delta g.\Delta \xi)$ in the spatial derivative terms. Applying equation (11) to each of the Euler equations, the final version is obtained as,

12

For mass conservation :

$$\frac{\partial}{\partial t}(\rho A)_{i,j} + \left[\frac{\partial \xi}{\partial x}\right]_{i,j} \cdot \left[ (\rho u S)_{i+1/2,j} - (\rho u S)_{i-1/2,j} \right]$$

$$+ \left[\frac{\partial \eta}{\partial y}\right]_{i,j} \cdot \left[ (\rho v S)_{i,j+1/2} - (\rho v S)_{i,j-1/2} \right] = 0 \qquad (12)$$

For x-momentum conservation :

$$\frac{\partial}{\partial t}(\rho u A)_{i,j} + \left[\frac{\partial \xi}{\partial x}\right]_{i,j} \cdot \left[ \{(\rho u^2 + p)S\}_{i+1/2,j} + p_b Y_p \right.$$

$$- \{(\rho u^2 + p)S\}_{i-1/2,j} \right] + \left[\frac{\partial \eta}{\partial y}\right]_{i,j} \cdot \left[ (\rho u v S)_{i,j+1/2} \right.$$

$$- (\rho u v S)_{i,j-1/2} \right] = 0 \qquad (13)$$

For y-momentum conservation :

$$\frac{\partial}{\partial t}(\rho v A)_{i,j} + \left[\frac{\partial \xi}{\partial x}\right]_{i,j} \cdot \left[ (\rho u v S)_{i+1/2,j} - (\rho u v S)_{i-1/2,j} \right]$$

$$+ \left[\frac{\partial \eta}{\partial y}\right]_{i,j} \cdot \left[ \{(\rho v^2 + p)S\}_{i,j-1/2} - p_b X_p \right.$$

$$+ \{(\rho v^2 + p)S\}_{i,j-1/2} \right] = 0 \qquad (14)$$

For energy conservation :

$$\frac{\partial}{\partial t}(\rho E A)_{i,j} + \left[\frac{\partial \xi}{\partial x}\right]_{i,j} \cdot \left[ (\rho u H S)_{i+1/2,j} - (\rho u H S)_{i-1/2,j} \right]$$

$$+ \left[\frac{\partial \eta}{\partial y}\right]_{i,j} \cdot \left[ (\rho v H S)_{i,j+1/2} - (\rho v H S)_{i,j-1/2} \right] = 0 \qquad (15)$$

13

where, with reference to Fig. 1, it can be seen that,

$$S_{i+1/2} = S_3 \quad , \quad S_{i-1/2} = S_1$$

$$S_{j+1/2} = S_4 \quad , \quad S_{j-1/2} = S_2$$

$$S_{i+1/2,j} - S_{i-1/2,j} = \Delta \eta = S_3 - S_1$$

$$S_{i,j+1/2} - S_{i,j-1/2} = \Delta \xi = S_4 - S_2$$

$$X_p = \Delta \xi = \text{x - projection of segment of airfoil surface}$$
$$\text{that is intersected by a boundary cell}$$

$$Y_p = \Delta \eta = \text{y - projection of this segment as above}$$

$$p_b = \text{pressure on body surface}$$

It can be noted from the above expressions that for the upstream facing side of the airfoil, the term $Y_p \leq 0$, thus ensuring a decrease in the horizontal flux and a corresponding increase in the vertical flux. Therefore, the velocity $v$ thus computed will show a physically logical increase on the upstream facing side of the airfoil. Similarly, for the downstream side of the airfoil, $Y_p \geq 0$, thus leading to the reverse of the above situation. For the lower surface of the airfoil, the term $X_p \leq 0$ and for the upper surface, $X_p \geq 0$.

Furthermore, if a finite volume cell is on the airfoil surface (i.e. a boundary cell), then the cell side that is intersected by the airfoil surface is set equal to zero. As an example, consider the boundary cell in Fig. 3 shown by dashed lines. Here, the cell side $S_2 = 0$ (following the notation of Fig. 1). This is according to the formulation proposed by Wedan and South (Ref. 16), which sets the zero--flux boundary condition on the solid wall of the airfoil surface. Thus the grid generation is indeed critical.

As a result of the finite volume discretization, equations (12), (13), (14) and (15) can be collectively expressed as a system of ordinary differential equations, by considering the grid to be invariant with respect to time, or,

14

$$\frac{d A_{i,j}}{d t} = 0$$

where $A_{i,j} = \Delta\xi.\Delta\eta$. Therefore, they can be written as,

$$\frac{d w_{i,j}}{d t} + \frac{F_{i,j}}{A_{i,j}} = 0 \tag{16}$$

where the term $w_{i,j}$ refers to the unknown variables as in equation (2). The time-marching procedure (a Runge-Kutta scheme) will be shown later in this chapter.

## § 2.5 Artificial Dissipation Calculations :

If Cartesian grids are used for the finite volume approach to the solution of an inviscid flow, then the problem is one of central differences on the Cartesian mesh. This is seen from the governing equations (12) - (15), derived earlier in this chapter. This central differencing scheme is characterized by 'wiggles' between the odd and even grid points and oscillations in regions of high pressure gradients, occuring around shock waves or stagnation points (e.g. at the leading edge, for subsonic lifting flow). For example, consider the model linearized one-dimensional flow, with negligible viscosity (viscosity coefficient $= \varepsilon$ ) described as,

$$\frac{\partial u}{\partial t} + c.\frac{\partial u}{\partial x} = \varepsilon.\frac{\partial^2 u}{\partial x^2} \tag{17}$$

Using central differences with a one-step explicit scheme, this can be written as follows,

$$\frac{u_i^{n+1} - u_i^n}{\Delta t} + c.\frac{u_{i+1}^n - u_{i-1}^n}{2.\Delta x} = \varepsilon.\frac{u_{i+1}^n - 2 u_i^n + u_{i-1}^n}{\Delta x^2} \tag{18}$$

Defining the cell Reynold's (or Peclet) Number as, $Re_{\Delta x} = c.\Delta x / \varepsilon$ and a coefficient r as, $r = \varepsilon.\Delta t / \Delta x^2$, then the equation (18) can be written as,

15

$$u_i^{n+1} = \frac{r}{2} \cdot (2 - Re_{\Delta x}) \cdot u_{i+1}^n + (1 - 2r) \cdot u_i^n$$

$$+ \frac{r}{2} \cdot (2 + Re_{\Delta x}) \cdot u_{i-1}^n \tag{19}$$

Now, it is desired that a steady-state solution be obtained for the above equation, at a high Reynold's Number - because the Euler equations are the approximation to the Navier-Stokes equations, in the limit of infinite Reynold's Number.

Therefore, given an initial condition as (Ref. 21),

$$u(x, 0) = 0, \qquad 0 \le x \le 1$$

and boundary conditions as,

$$u(0, t) = 0 \quad ; \quad u(1, t) = 1$$

the behaviour of $u_i^{n+1}$ can be studied from equation (19), using a 11-point grid, for example. At the end of the first time step, the values of $u_i^{n+1} = 0$, at all $i$ grid locations except at $i = 10$ and $i = 11$ where,

$$u_{10}^{n+1} = \frac{r}{2} \cdot (2 - Re_{\Delta x}) \cdot (1) + (1 - 2r) \cdot (0) + \frac{r}{2} \cdot (2 + Re_{\Delta x}) \cdot (0)$$

$$= \frac{r}{2} \cdot (2 - Re_{\Delta x}) \tag{20}$$

and $u_{11}$ is fixed at 1, on the boundary.

In equation (20), if the cell Reynolds Number $Re_{\Delta x}$ is increased beyond 2,

$$u_{10}^{n+1} < 0 \quad ; \qquad \text{this is an even point oscillation}$$

At the second time step, using the same value of $Re_{\Delta x} > 2$, this oscillation will propagate upstream by one point, as from equation (20),

$$u_9^{n+2} = \frac{r}{2} \cdot (2 - Re_{\Delta x}) \cdot u_{10}^{n+1}$$

$$> 0 \quad ; \qquad \text{this is an odd point oscillation}$$

16

Thus, at subsequent time steps, these 'wiggles' between odd and even points will keep on propagating upstream and will exist even at steady-state, due to the second-order truncation error of the central difference scheme used for the convective term in the equation (17). This can be corrected by using an upwind difference for this convective term, or equivalently, adding artificial dissipation terms to the convective term.

However, as shown below, upwind differencing schemes are not always stable. Consider a purely inviscid version of equation (17) with a first order backward difference for the convective term as,

$$\frac{u_i^{n+1} - u_i^n}{\Delta t} + \lambda' \cdot \frac{u_i - u_{i-1}}{\Delta x} = 0 \qquad (21)$$

A Fourier analysis of equation (21) can be carried out for studying the stability of this scheme, by considering,

$$u_i^n = e^{at} \cdot e^{jkx}, \qquad \text{where } j = (-1)^{1/2}$$

The amplification factor is then obtained as,

$$z = e^{a\Delta t} = 1 + \left\{ -\lambda' \frac{\Delta t}{\Delta x} \cdot [2.\sin^2(\theta/2) + j\sin\theta] \right\} \qquad (22)$$

where, $\theta = k.\Delta x$.

Hence for stability of this scheme, it is required that,

$$|z| \leq 1 \qquad \text{or} \qquad \lambda' > 0 \qquad (23)$$

But, as is analyzed later in this chapter, the Euler equations have both positive and negative eigenvalues. Hence the backward difference used in equation (21) can be unstable for negative eigenvalues, except when flux-splitting of the convective terms is resorted to, in the Euler equations. Therefore, for positive eigenvalues, the first order backward difference of equation (21) is used and by an analysis similar to equations (22) and (23), it can be shown that, for negative eigenvalues, the first order forward

17

difference $(u_{i+1} - u_i)$ can be a stable representation for $\Delta u$.

Now, it is necessary to show the equivalence between the implicit dissipation of an upwind scheme and the dissipation added explicitly to the second-order central difference terms of the finite volume scheme followed in this thesis.

A second-order central difference form of the convective term $\partial u / \partial x$ can be written as,

$$\frac{u_{i+1} - u_{i-1}}{2.\Delta x} = \frac{u_i - u_{i-1}}{\Delta x} + \frac{1}{2.\Delta x}(u_{i+1} - 2.u_i + u_{i-1}) \qquad (24)$$

$$\text{or,} \quad \delta_1^b = (u_i - u_{i-1})/\Delta x = \delta_1 + (\Delta x / 2).u_{xx}$$

$$= 2^{nd} \text{ order central difference } + \text{ Dissipation} \qquad (25)$$

where the second-order central difference is,

$$(\delta_1^b + \delta_1^f)/2$$

and the dissipation is a second order difference,

$$D^2 = \frac{-1}{2.\Delta x}(u_{i+1} - 2.u_i + u_{i-1})$$

$$= -(\delta_1^b - \delta_1^f)/2 \qquad (26)$$

where, $\delta^b$ and $\delta^f$ are denoting the backward and forward differences, respectively.

Next, the second order upwind and forward difference formulas can be written as,

$$\delta_2^b = \frac{\partial u}{\partial x} = \frac{3.u_i - 4.u_{i-1} + u_{i-2}}{2.\Delta x} \qquad \text{and}$$

$$\delta_2^f = \frac{-3.u_i + 4.u_{i+1} - u_{i+2}}{2.\Delta x} \qquad (27)$$

18

Thus, another form of a second order central difference formula for the convective term can be written in a way similar to equation (25) as,

$$(\delta_2^b + \delta_2^f)/2 = \frac{-u_{i+2} + 4.u_{i+1} - 4.u_{i-1} + u_{i-2}}{4.\Delta x}$$

$$= \delta_2^b - \text{Dissipation} \tag{28}$$

or, $\delta_2^b = \delta_2 + (\Delta x^3/4).u_{xxxx}$

$$= 2^{nd} \text{ order central difference} + \text{Dissipation} \tag{29}$$

where the dissipation is the fourth order difference,

$$D^4 = \frac{1}{4.\Delta x}.(u_{i+2} - 4.u_{i+1} + 6.u_i - 4.u_{i-1} + u_{i-2})$$

or, $D^4 = (\delta_2^b + \delta_2^f)/2$ \hfill (30)

Hence, equation (25) shows that a first order upwind scheme produces the equivalent of explicitly adding a second difference dissipation $D^2$ to a second order central difference. Similarly, equation (29) shows that a second order upwind scheme can be equivalent to explicitly adding a fourth difference dissipation $D^4$ to a central difference scheme of second order.

Now the problem is to switch between the second difference and fourth difference dissipations, in the vicinity of a shock wave. This can be studied by considering the following problem (Ref. 22),

$$\frac{\partial u}{\partial t} + \frac{\partial u}{\partial x} = 0 \tag{31}$$

assuming for simplicity, a grid of mesh size, $\Delta x = 1$ and time step, $\Delta t = 1$,

19

given the initial conditions as a shock - like profile,

$$u_i^{n+1} = 1, \quad i \leq I - 1$$
$$= 0, \quad i = I$$
$$= -1, \quad i \geq I + 1 \tag{32}$$

Let the updated value after one time step be expressed as,

$$u_i^{n+1} = u_i^n - \left(\frac{u_{i+1}^n - u_{i-1}^n}{2}\right) + D_i \tag{33}$$

The term $D_i$ is a dissipation operator based on the expressions derived in equations (26) and (30) as,

$$D_i = D_i^4 = -0.25 \cdot (u_{i+2}^n - 4.u_{i+1}^n + 6.u_i^n - 4.u_{i-1}^n + u_{i-2}^n) \tag{34a}$$

$$= D_i^2 = 0.5 \cdot (u_{i+1}^n - 2.u_i^n + u_{i-1}^n) \tag{34b}$$

Using the fourth difference dissipation $D^4$, the solution after one time step is seen to have an overshoot ($= 1.25$) before the shock, at $i = I - 2$ and a corresponding undershoot ($= -1.25$) after the shock, at $i = I + 2$. On the other hand, the second difference dissipation $D^2$ allows the initial condition to propagate exactly, without any oscillations before and after the shock (Ref. 23). However, as analyzed earlier, this dissipation $D^2$ when combined with central differences, produces only a first order accurate upwind scheme. Therefore, in order to have second order accuracy in upwinding, the $D^4$ dissipation should be used everywhere, except in the vicinity of shocks - where the $D^2$ dissipation should be switched on.

The dissipation terms are computed at each cell $(i, j)$, separately in the $x$ and $y$ directions. Considering the mass continuity equation for example, it is seen that,

20

$$D\rho \quad = \quad D_x\rho \quad + \quad D_y\rho \tag{35}$$

where (Refs. 24 to 29),

$$D_x\rho \quad = \quad d_{i+1/2,j} \; - \; d_{i-1/2,j}$$

$$D_y\rho \quad = \quad d_{i,j+1/2} \; - \; d_{i,j-1/2} \tag{36}$$

All the terms on the right hand side of equation (36) have a similar form. For example,

$$d_{i+1/2,j} \quad = \quad \frac{A_{i+1/2,j}}{\Delta t_{i+1/2,j}} \cdot [\, \varepsilon^{(2)}_{i+1/2,j} \cdot (\rho_{i+1,j} - \rho_{i,j})$$
$$- \; \varepsilon^{(4)}_{i+1/2,j} \cdot (\rho_{i+2,j} - 3\cdot\rho_{i+1,j} + 3\cdot\rho_{i,j} - \rho_{i-1,j})]\,. \tag{37}$$

$$d_{i-1/2,j} \quad = \quad \frac{A_{i-1/2,j}}{\Delta t_{i-1/2,j}} \cdot [\, \varepsilon^{(2)}_{i-1/2,j} \cdot (\rho_{i,j} - \rho_{i-1,j})$$
$$- \; \varepsilon^{(4)}_{i-1/2,j} \cdot (\rho_{i+1,j} - 3\cdot\rho_{i,j} + 3\cdot\rho_{i-1,j} - \rho_{i-2,j})] \tag{38}$$

The values on the cell side $(i+1/2, j)$ for example, are averaged as,

$$\rho_{i+1/2,j} \quad = \quad \tfrac{1}{2} \cdot (\rho_{i,j} + \rho_{i+1,j})$$

Likewise, $\Delta t_{i+1/2,j}$ and $A_{i+1/2,j}$ are averages of the time steps and the areas of the two cells $(i, j)$ and $(i+1, j)$. The equations (37) and (38) are denoting a rate of change of mass, dimensionally corresponding to equation (16).

It is interesting to note from equations (37) and (38) that the $D^2$ and $D^4$ dissipations have opposite signs, so that positive damping can be implemented in equation (16). This is also seen in equations (25) and (29). The term $A_{i+1/2,j}$ is of order $(\Delta x)$ and the second difference between two cells is of order $(\Delta x)$. The fourth difference between four cells is of order $(\Delta x)^3$, if the coefficients $\varepsilon^{(2)}$ and $\varepsilon^{(4)}$ are each of order unity. However these coefficients can be adapted to the flow. To achieve this,

the coefficient $\varepsilon^{(2)}$ should be of order $(\Delta x)^2$, so the whole expression and hence the quantities $d_{i+1/2,j}$ and $d_{i-1/2,j}$ will both be of order $(\Delta x)^4$. This means that an error term of only third order is being added to the spatial differencing operator $F_{i,j}$ for the convective terms in the equation (16). Therefore, this third order error is a mixture of second and fourth differences. An effective sensor of the presence of a shock wave can be devised by taking the second difference of the pressure, corresponding to the second order accuracy of the central differences for the convective terms. The coefficients $\varepsilon^{(2)}$ and $\varepsilon^{(4)}$ are then obtained as,

$$\varepsilon^{(2)}_{i+1/2,j} = k^{(2)} . \text{Max} (v_{i,j}, v_{i+1,j}) \tag{39}$$

$$\varepsilon^{(4)}_{i+1/2,j} = \text{Max} [0, (k^{(4)} - \varepsilon^{(2)}_{i+1/2,j})] \tag{40}$$

where,

$$v_{i,j} = \frac{|p_{i+1,j} - 2.p_{i,j} + p_{i-1,j}|}{|p_{i+1,j}| + 2.|p_{i,j}| + |p_{i-1,j}|} \tag{41}$$

and $k^{(2)} = 1/4$ ; $k^{(4)} = 1/256$.

The arbitrary constants $k^{(2)}$ and $k^{(4)}$ are empirically chosen, as proposed in Ref. (24). From equation (40), it is seen that the coefficient $\bar{\varepsilon}^{(4)}$ is of order 1. The second difference is multiplied by a coefficient $\varepsilon^{(2)}$ which is of order $(\Delta x)^2$ in subsonic flow, increasing to order 1 in the vicinity of a shock wave. As for the fourth difference, it is multiplied by a coefficient $\varepsilon^{(4)}$ of order 1 in subsonic flow, falling to zero through a shock. As these flow-adaptive coefficients depend on the grid spacing, it is easily seen that a medium to fine grid should be used, in order to use as little dissipation as possible. The dissipative terms for the momentum and energy equations are constructed in the same way as done for the continuity equation, by substituting $\rho u$, $\rho v$ and $\rho E$ in that order, for $\rho$ in equations (37) and (38).

As can be seen from equations (37) and (38), the evaluation of the dissipation terms

22

poses some problems both at the airfoil surface and at the far-field boundaries, regarding 'ghost' cells. The far-field treatment will be discussed later. At the airfoil surface, only one set of boundary cells (i, j) are available. In order to obtain values at the cell (i, j-1), designated as cell g1 and at the cell (i, j-2) designated as cell g2, second order extrapolation is carried out in the vertical direction as (see Fig. 30),

$$w_{g1} = 2.w_{i,j} - w_{i,j+1}$$

$$w_{g2} = 2.w_{i,j-1} - w_{i,j} \tag{42}$$

where {w} denotes the primitive variables $\rho$, u, v, p and E.

Lastly, it is worth noting how the damping produced by the dissipation terms can be interpreted physically. Consider equation (16) with fourth-order dissipation introduced as in equation (29), for a finite volume cell in one-dimensional space,

$$w_{,t} = -\frac{F(w)}{A} - \frac{1}{A} . (K^4 w_{xx})_{xx} \tag{43}$$

where $K^4 = \epsilon^{(4)} . A / \Delta t$, as seen in equations (37) and (38) and A = cell area. Multiplying both sides of equation (43) by w and integrating with respect to x, it is seen that (Ref. 30),

$$\frac{1}{2} . \frac{d}{dt} \int |w|^2 \, dx = \int \frac{w}{A} . [-F(w)] \, dx - \frac{1}{A} . \int w.(K^4 w_{xx})_{xx} \, dx \tag{44}$$

Integrating the second term on the right hand side of equation (44), twice by parts with respect to x, it is seen that,

$$\frac{1}{2} . \frac{d}{dt} \int |w|^2 \, dx = \int \frac{w}{A} . [-F(w)] \, dx - \frac{1}{A} . \int K^4 . (w_{xx})^2 \, dx \tag{45}$$

23

where $K^4 > 0$ means that the artificial viscosity terms decrease the total energy of the finite volume system. Hence this helps in accelerating the convergence of the unsteady equations to the steady state.

## § 2.6 Time-Stepping Procedure :

The unsteady term in equation (16) has to be integrated with respect to time. After addition of the dissipation terms $D_{i,j}$, equation (16) is modified to,

$$\frac{dw}{dt} + R(w) = 0 \qquad (46)$$

where $R(w)$ is the residual,

$$R_{i,j} = \frac{1}{A_{i,j}} \cdot (F_{i,j} - D_{i,j}) \qquad (47)$$

The simplest time-stepping scheme is the Euler explicit method (forward time and centered space) which is unstable as shown in equations (18), (19) and (20). It can be made stable by replacing $u_i$ in the linearized one-dimensional wave equation,

$$\frac{\partial u}{\partial t} + c \cdot \frac{\partial u}{\partial x} = 0 \qquad (48a)$$

by,

$$u_i = \frac{1}{2} \cdot (u_{i+1} + u_{i-1}) \qquad (48b)$$

However, this will be only first-order accurate in time. A Fourier stability analysis of equation (48) can be carried out by considering,

$$u_i^n = e^{at} \cdot e^{jkx}, \qquad \text{where } j = (-1)^{1/2}$$

from which it is seen that the amplification factor is obtained as,

$$z = e^{a\Delta t} = \cos\theta - j\lambda.\sin\theta ,$$

24

where, $\theta = k.\Delta x$ and $\lambda = c.\Delta t / \Delta x = $ Courant Number.

For stability of the scheme in equation (48), $|z| \leq 1$ or $\lambda \leq 1$.

Obviously, this is a limitation on both the time-accuracy and the Courant Number.

The next explicit scheme is the two-step Lax-Wendroff method given as,

$$u_{i+1/2}^{n+1/2} = \frac{1}{2} \cdot (u_i^n + u_{i+1}^n) - \frac{\lambda}{2} \cdot (u_{i+1}^n - u_i^n)$$

$$u_i^{n+1} = u_i^n - \lambda \cdot (u_{i+1/2}^{n+1/2} - u_{i-1/2}^{n+1/2}) \tag{49}$$

where $\lambda = c.\Delta t / \Delta x = $ Courant Number.

Upon taking Taylor's series expansions for space and time, it is seen that the truncation error for this Lax-Wendroff scheme is of the order of. $(\Delta x)^2$ and $(\Delta t)^2$. The main drawback of this method is the need to compute unknowns at the two grid points $i+1/2$ and $i-1/2$.

This is rendered unnecessary by considering another well known two-step method with second-order spatial accuracy - the explicit predictor-corrector MacCormack scheme,

$$\bar{u}_i^{n+1} = u_i^n - \lambda.(u_{i+1}^n - u_i^n)$$

$$u_i^{n+1} = \frac{1}{2} \cdot (u_i^n + \bar{u}_i^{n+1}) - \frac{\lambda}{2} \cdot (\bar{u}_i^{n+1} - \bar{u}_{i-1}^{n+1}) \tag{50}$$

The stability limits for both the Lax-Wendroff and the MacCormack schemes are the same, $\lambda \leq 1$.

The simplest second-order time accurate method is the Leap Frog scheme. When this is applied to equation (48a), it is seen that,

$$\frac{u_i^{n+1} - u_i^{n-1}}{2.\Delta t} + c.\frac{u_{i+1}^n - u_{i-1}^n}{2.\Delta x} = 0 \qquad (51)$$

It is seen from equations (49) and (51) that the second step of the Lax-Wendroff method is equal to the Leap Frog method for the remaining half time step. The Leap Frog method is better than the Lax-Wendroff method in one way - that it does not need an additional step to accomplish second order time accuracy. However, the main drawback of the Leap-Frog method is the need to have a special starting procedure for obtaining the values at the $(n-1)^{th}$ time step.

All the above schemes are only $(\Delta t)^2$ accurate and have a limit on Courant Number as 1. Therefore it is necessary to search for a scheme with a higher order of time accuracy. The classical four step Runge-Kutta scheme has the advantage of being time accurate to the order of $(\Delta t)^4$. Any four stage time-stepping scheme can be studied by expanding $u_i^{n+1}$ in a Taylor's series as,

$$u_i^{n+1} = u_i^n + \Delta t.\frac{\partial u}{\partial t} + \frac{(\Delta t)^2}{2!}.\frac{\partial^2 u}{\partial t^2} + \frac{(\Delta t)^3}{3!}.\frac{\partial^3 u}{\partial t^3}$$
$$+ \frac{(\Delta t)^4}{4!}.\frac{\partial^4 u}{\partial t^4} + \cdots \qquad (52)$$

where the term $u_t (= \partial u / \partial t)$ is obtained from equation (48a) as,

$$u_t = -c.u_x , \quad \text{leading to}$$

$$u_{xt} = -c.u_{xx} \qquad (53a)$$

$$u_{tt} = -c.u_{xt} \qquad (53b)$$

Substituting for $u_{xt}$ from equation (53a) into equation (53b), it is seen that,

$$u_{tt} = c^2.u_{xx} \qquad (54a)$$

Similarly,

26

$$u_{ttt} = -c^3 . u_{xxx} \qquad (54b)$$

$$u_{tttt} = c^4 . u_{xxxx} \qquad (54c)$$

Upon substituting for $u_t$, $u_{tt}$, $u_{ttt}$ and $u_{tttt}$ from equations (48a), (54a), (54b) and (54c), into the equation (52), the following is obtained as,

$$u_i^{n+1} = u_i^n - \lambda . \delta u + \frac{\lambda^2}{2!} . \delta^2 u - \frac{\lambda^3}{3!} . \delta^3 u + \frac{\lambda^4}{4!} . \delta^4 u - \cdots \qquad (55)$$

where the terms in $\delta$, $\delta^2$, $\delta^3$ and $\delta^4$ are the familiar central difference terms of second order accuracy and $\lambda = c.\Delta t / \Delta x =$ Courant Number.

Putting Fourier terms into equation (55) as,

$$u_i^{n+1} = e^{at} . e^{jk(x+\Delta x)} , \qquad \text{where} \quad j = (-1)^{1/2}$$

it is seen that the amplification factor obtained is a polynomial in $z$ [ $= \lambda . j \sin(k.\Delta x)$ ],

$$G(z) = e^{a\Delta t} = 1 + A_1 . z + A_2 . z^2$$
$$+ A_3 . z^3 + A_4 . z^4 + \cdots \qquad (56)$$

The stability region of such a fourth-order scheme is given by those values of $z$ for which the amplification factor, $G(z) \leq 1$.

Consider the model problem of equation (48a) with second-difference dissipation,

$$\frac{\partial u}{\partial t} = -c . \frac{\partial u}{\partial x} + \varepsilon^{(2)} . (\Delta x)^2 . \frac{\partial^2 u}{\partial x^2} \qquad (57)$$

Introducing central difference approximations and a Fourier term as before, the amplification factor is obtained as,

$$e^{a\Delta t} = j(-\lambda . \sin\theta) + (1 - 4.\varepsilon^{(2)} . \sin^2\theta / 2) \qquad (58)$$

where $j = (-1)^{1/2}$, $\theta = k.\Delta x$ and $\lambda = c.\Delta t / \Delta x$ = Courant Number.

The stability region is given by a plot of values of $\theta$ for which $|e^{a\Delta t}| \leq 1$. It can be seen from equation (58) that the addition of the dissipation terms shifts the stability region to the left of the real axis, while the maximum value of the intercept on the imaginary axis gives the value of the Courant Number $\lambda$ for which the time-stepping scheme will be stable. A similar treatment of equation (56) shows that the Courant Number of any fourth order scheme is given by the intercept of the stability region with the imaginary axis and has been found to be equal to about 2.8 by Jameson and others (Refs. 24 to 30). Therefore, in comparison with all the first and second-order time-stepping schemes examined so far, the classical fourth-order Runge-Kutta procedure has the advantage of :

(a) Higher order of time accuracy $[ = (\Delta t)^4 ]$ and

(b) Higher value of Courant Number $[ = 2.8 ]$.

Moreover, in contrast to the Leap Frog scheme and an alternative fourth-order scheme like the Adams-Bashforth method, the four-step Runge-Kutta method does not require any special starting procedures for getting initial values of the unknown variable at previous time steps. Applying this classical four-step Runge-Kutta method to equation (46) gives,

$$
\begin{aligned}
w^{(0)} &= w^n \\
w^{(1)} &= w^{(0)} - (\Delta t / 2). R(w^{(0)}) \\
w^{(2)} &= w^{(1)} - (\Delta t / 2). R(w^{(1)}) \\
w^{(3)} &= w^{(2)} - (\Delta t / 2). R(w^{(2)}) \\
w^{(4)} &= w^{(3)} - (\Delta t / 6).[R(w^{(0)}) + 2.R(w^{(1)}) + 2.R(w^{(2)}) + R(w^{(3)})] \\
w^{n+1} &= w^{(4)}
\end{aligned}
\tag{59}
$$

where $R(w)$ is obtained from equation (47). However, one drawback of this classical type of four-step Runge-Kutta method is the need to store the values of the variable $w$.

at each of the four steps 0, 1, 2 and 3 in order to compute the final value at the fourth step. This becomes a serious computer storage problem, especially since $w^n$ denotes the Euler variables $\rho$, $\rho u$, $\rho v$ and $\rho E$.

Therefore, alternative forms of this classical procedure have been studied by Jameson in Ref. (28) and by Turkel in Ref. (30), which have been found to have the same Courant Number ( = 2.8) and time accuracy of the order of $(\Delta t)^4$ as the classical form. One such scheme which is used in this thesis is given as,

$$
\begin{aligned}
w^{(0)} &= w^n \\
w^{(1)} &= w^{(0)} - (1/4).\Delta t . R(w^{(0)}) \\
w^{(2)} &= w^{(1)} - (1/3).\Delta t . R(w^{(1)}) \\
w^{(3)} &= w^{(2)} - (1/2).\Delta t . R(w^{(2)}) \\
w^{(4)} &= w^{(3)} - \Delta t . R(w^{(3)}) \\
w^{n+1} &= w^{(4)}
\end{aligned}
\tag{60a}
$$

where $R(w)$ is obtained from equation (47). In this case, evaluation of the dissipation terms $D(w)$ at each of the four steps of the Runge-Kutta scheme, will require a large amount of computer time. It has already been shown in the analysis leading to the equations (39) and (40), that the dissipation terms are contributing an error term of only third order to the convective terms. Therefore, a considerable amount of computer time can be saved by freezing the dissipation terms at their values before the start of the first step of the Runge-Kutta scheme. As a result of this, the terms $R(w^{(k)})$ in each step $k = 1, 2, 3, 4$ can be written for a finite volume cell (i, j) as,

$$
R(w^{(k)}) = \frac{1}{A_{i,j}} . [ F(w^{(k)}) - D(w^{(0)}) ]
\tag{60b}
$$

Summarizing the time-stepping procedures examined above, after Jameson (Ref. 2.10), it is seen that if one unit of work is assigned to the operators $F$ and $D$ of equation (47),

then the following table illustrates their respective merits and demerits :

| Procedure | F | D | Work | Cour. # | Efficiency = Cour. # / Work |
|-----------|---|---|------|---------|------------------------------|
| Leap Frog | 1 | 1 | 2 | 1 | 0.5 |
| MacCormack | 2 | 1 | 3 | 1 | 0.3 |
| LaxWendroff | 2 | 1 | 3 | 1 | 0.3 |
| R-K (eqn. 60a) | 4 | 4 | 8 | 2.8 | 0.35 |
| R-K (eqn. 60b) | 4 | 1 | 5 | 2.8 | 0.56 |

Hence, although a fourth order Runge-Kutta scheme using equation (60b) was followed in the present work, it is possible to use other methods like the Lax-Wendroff and the MacCormack schemes, where the maximum Courant Number is limited by the number of steps within a particular scheme. Since all the methods reviewed are of the explicit sort, it is obvious that Courant Number restrictions can be overcome by using implicit methods, which on the other hand, have the drawbacks of more computation and storage.

Therefore, explicit methods require an estimate of the local time step $\Delta t$. Consider the two-dimensional form of the linear inviscid flow equation (48a) as,

$$\frac{\partial u}{\partial t} + c.\frac{\partial u}{\partial x} + c.\frac{\partial u}{\partial y} = 0 \tag{61}$$

Using second-order central difference forms of the flux terms and a simple explicit time-stepping scheme, it is seen that,

$$u_{i,j}^{n+1} = u_{i,j}^{n} + \frac{c.\Delta t}{2.\Delta x}(u_{i+1,j}^{n} - u_{i-1,j}^{n}) + \frac{c.\Delta t}{2.\Delta y}(u_{i,j+1}^{n} - u_{i,j-1}^{n}) \tag{62}$$

Introducing a Fourier term into the above equation (62) as,

$$u_{i,j}^{n} = e^{at}.e^{Jkx}.e^{Jky} \quad , \quad \text{where} \quad J = (-1)^{1/2}$$

30

the following expression for the amplification factor is obtained as,

$$e^{a\Delta t} \quad = \quad 1 - J (\lambda_x . \sin \theta_x + \lambda_y . \sin \theta_y) \tag{63}$$

where,

$\lambda_x$ and $\lambda_y$ are the Courant Numbers in the x- and y-directions and

$$\theta_x = k\Delta x \quad , \quad \theta_y = k\Delta y$$

The maximum value of the imaginary part of the amplification factor in equation (63) is obtained when,

$$\theta_x = \pi/2 = \theta_y$$

For stability it is necessary that $|e^{a\Delta t}| \leq 1$, which leads to,

$$\lambda_x + \lambda_y \leq 1 \tag{64}$$

In the analysis of the boundary conditions, it will be shown that the maximum eigenvalues in the x- and y-directions are obtained as $|u| + c'$ and $|v| + c'$ respectively, where $c' =$ speed of sound. Therefore $\lambda_x$ and $\lambda_y$ are maximum when,

$$\lambda_x = (|u| + c').\frac{\Delta t}{\Delta x} \quad ; \quad \lambda_y = (|v| + c').\frac{\Delta t}{\Delta y} \tag{65}$$

Substituting for $\lambda_x$ and $\lambda_y$ from equation (65) into equation (64), it is seen that,

$$\frac{1}{\Delta t_x} + \frac{1}{\Delta t_y} \leq \frac{1}{\Delta t} \tag{66}$$

where,

$$\Delta t_x = \frac{\Delta x}{(|u| + c')} \quad , \quad \Delta t_y = \frac{\Delta y}{(|v| + c')} \tag{67}$$

are the time steps in the x- and y-directions respectively, where,

31

$$\Delta x = \frac{\Delta\xi}{(\partial\xi/\partial x)} \quad , \quad \Delta y = \frac{\Delta\eta}{(\partial\eta/\partial y)}$$

with $(\partial\xi/\partial x)$ and $(\partial\eta/\partial y)$ being given by equation (6b). Equation (66) is used to obtain the value of the resultant local time step and is valid only for a Courant Number (CN) of 1, irrespective of the time-stepping procedure followed. Since the overall Courant Number depends on the particular time-stepping scheme, it follows that,

$$\lambda_x = CN = \lambda_y \tag{68}$$

Putting equation (68) into equation (65), it is seen that the time steps in equation (67) are multiplied by a factor equal to CN ($= 2.8$, for the fourth order Runge-Kutta scheme).

In order to examine the effect of using a local time step instead of a fixed minimum $\Delta t$ for the time-stepping procedure, it is useful to recall the second order wave equation given by equation (54a) as,

$$u_{tt} = c^2 . u_{xx} \quad , \quad \text{where } c = \text{linearized wave speed}$$

Using central differences to discretize the time variable, it is seen that,

$$\frac{u_i^{n+1} - 2.u_i^n + u_i^{n-1}}{(\Delta t)^2} = c^2 . u_{xx} \tag{69}$$

where $\Delta t$ = local time step. If a minimum time step $(\Delta t)_{min.}$ is chosen, then the equation (69) results in,

$$\frac{u_i^{n+1} - 2 u_i^n + u_i^{n-1}}{(\Delta t)_{min.}^2} = p^2 . c^2 u_{xx} \tag{70}$$

where,

$$p = \frac{\text{local time step, } \Delta t}{(\Delta t)_{min.}} \quad \alpha \quad \frac{\Delta x}{(\Delta x)_{min.}}$$

32

with $\Delta x$ denoting the grid size. Hence, using a local time step is equivalent to increasing the wave speed $c$ to $(p \cdot c)$ and this factor $p$ increases upon going towards the far-field boundary, where the cells are highly stretched as compared to cells near the airfoil. Therefore, since the disturbances are carried away towards the far-field at a speed equal to the wave speed $c$, it follows that using a local time step is a method of accelerating the convergence rate - although at a reduced Courant Number of 1.

## § 2.7 Boundary Conditions :

At the solid boundary of the airfoil surface, the zero normal flux condition can be easily implemented by setting the length of the finite volume cell side that intersects the boundary, as equal to zero. Therefore, the only contribution to the flux balance will come from the body pressure $p_b$. If a body-fitted grid is being used, then it is necessary to use the normal momentum equation,

$$\frac{\partial p}{\partial n} = \frac{-\rho \cdot q^2}{\kappa} \tag{71}$$

where $q$ is the velocity tangential to the airfoil surface and $\kappa$ is the radius of curvature. Since a simple Cartesian grid is being used in the present work, the body pressure can be evaluated using second-order extrapolation in the vertical direction, from neighbouring full cells in the following way (see Fig. 2),

$$p_b = p_{i,j} + \frac{ETAD}{\Delta \eta} \cdot (p_{i,j} - p_{i,j+1}) \tag{72}$$

where,

$$ETAD = \frac{1}{2} \cdot (S_3 + S_1 - \Delta \eta) , \text{ for the boundary cell } (i, j) \text{ in Fig. 2}$$

Methods of implementing the far-field boundary conditions are discussed in Refs. (24), (31) and (32). In Ref. (24), Jameson draws a parallel with internal flow calculation

33

procedures, wherein the pressure at the exit of the channel is specified. This is because, at the outflow it is required that,

$$\frac{\partial p}{\partial y} = 0 \qquad (73a)$$

that is,

$$p = p_\infty \quad , \quad \text{freestream conditions} \qquad (73b)$$

Also, in Ref. (24) it is suggested that the density be computed after specifying the enthalpy H at its freestream values at the far-field boundaries. If the grid is very highly stretched, it might not be a problem to set freestream conditions everywhere on the boundary.

In the analysis leading to equation (70), it was shown that the wave speed of the second-order wave equation increases towards the far-field boundary. Therefore, the Euler equations being hyperbolic partial differential equations, the boundary conditions at the far-field are based on the signs and magnitudes of the characteristic wave speeds. The following analysis is based on the procedure followed in Ref. (17). Consider the inflow and outflow boundaries which are normal to the x-direction. Here, it can be assumed that the $\partial / \partial y$ derivatives that are tangent to these boundaries are negligible. Accordingly, the Euler equations (1) reduce to,

$$\frac{\partial w}{\partial t} + \frac{\partial f}{\partial x} = 0 \qquad (74)$$

where the vectors w and f are given as in equation (2).

The equation of state (3b) for an ideal gas can be written as,

$$p = \rho . (\gamma - 1) . c_v . T$$

and together with the relation between the total energy per unit volume $\rho E$ and the internal energy per unit mass $c_v T$,

$$\rho E = \rho.c_v.T + \frac{\rho u^2}{2} + \frac{\rho v^2}{2}$$

it can be expressed in terms of the four main conserved variables $\rho$, $\rho u$, $\rho v$ and $\rho E$ as,

$$p = (\gamma - 1).[\rho E - \frac{(\rho u^2)}{2.\rho} - \frac{(\rho v^2)}{2.\rho}] \tag{75}$$

As a result of this, the flux vector $f$ in equation (76) becomes a homogenous function of degree one in $w$ [ see equation (2) ], that is,

$$f(a.w) = a.f(w) , \quad \text{for any constant } a$$

Now, it is a property of homogenous functions that,

$$f = A.w , \quad \text{where} \quad A = \partial f / \partial w$$

Therefore, equation (74) can be written in conservative form as,

$$\frac{\partial w}{\partial t} + [A].\frac{\partial w}{\partial x} = 0 \tag{76}$$

The above equation (76) can also be written in non-conservative form as,

$$\frac{\partial w'}{\partial t} + [A'].\frac{\partial w'}{\partial x} = 0 \tag{77}$$

where,

$$w' = [\rho, u, v, p]^T = \text{vector of primitive variables} \tag{78}$$

and,

$$[A'] = \begin{bmatrix} u & \rho & 0 & 0 \\ 0 & u & 0 & 1/\rho \\ 0 & 0 & u & 0 \\ 0 & \gamma.p & 0 & u \end{bmatrix} \tag{79}$$

35

Now, for finding non-trivial eigenvalues $\lambda'$ of the Jacobian matrix $[A']$ of equation (79), it is required that,

$$\text{Determinant}[A' - \lambda'.I] = 0 \qquad (80)$$

where $[I]$ = the $(4 \times 4)$ identity matrix. Therefore, by putting equation (79) into equation (80), it is seen that,

$$(u - \lambda')^2.[(u - \lambda')^2 - \gamma.p/\rho] = 0 \qquad (81)$$

Solving this quartic equation (81) for $\lambda'$, the following solutions are obtained for the eigenvalues as,

$$\lambda' = u, \; u, \; u + c', \; u - c' \qquad (82)$$

where $c'^2 = \gamma.p/\rho$. It is seen from equation (82) that all the eigenvalues $\lambda'$ are real, since the Euler equations are hyperbolic equations.

Consider subsonic $(u < c')$ inflow in the x-direction. In this case, it is seen from equation (82) that three eigenvalues $u$, $u$ and $u + c'$ are positive, while one eigenvalue $u - c'$ is negative. This is shown in Fig. (5a), where three eigenvalues (positive) are coming in from the left and one eigenvalue (negative) is going out from the right, with reference to the inflow boundary of the computational domain. Hence, three characteristic variables can be specified (set equal to freestream conditions) and one variable must be extrapolated from interior values - at the inflow boundary. On the other hand, consider subsonic $(u < c')$ outflow as shown in Fig. (5b). Three positive eigenvalues are going out of the computational domain from the left and one eigenvalue is coming in from the right. So, three variables must be extrapolated and one variable must be specified at the outflow boundary.

It is known from gas dynamic principles that the Riemann invariants $R^+$ and $R^-$ are characteristic variables. Also [see equation (73a)], it is seen that at at a farfield boundary, it is required that $\partial p / \partial y = 0$. Substituting equation (73a) into the Euler y-momentum equation (1), leads to,

$$\frac{Dv}{Dt} = 0 \quad , \text{ at the outflow boundary} \tag{83}$$

i.e. at the outflow, the velocity $v$ is conserved along a streamline. Similarly, it is known that the entropy $S$ is conserved along a streamline, meaning that changes of state are adiabatic. Hence $v$ and $S$ are taken to be characteristic variables at the far-field boundaries.

At an inflow boundary, the specified and extrapolated Riemann invariants respectively are,

$$R_\infty = R^+ = u_\infty + \frac{2 . c'}{(\gamma - 1)} \quad \text{and}$$

$$R_e = R^- = u_e - \frac{2 . c'}{(\gamma - 1)} \tag{84a}$$

Similarly at the outflow boundary,

$$R_\infty = R^- \quad \text{and} \quad R_e = R^+ \tag{84b}$$

From either of equations (84a) and (84b), it is seen that,

$$u_{boundary} = (R_\infty + R_e)/2$$

$$= \frac{(u_\infty + u_e)}{2} + \frac{1}{(\gamma - 1)}(c'_\infty - c'_e) \tag{85}$$

and,

37

$$c_{boundary} = \frac{(\gamma - 1)}{4} \cdot (R_\infty - R_e)$$

$$= \frac{(\gamma - 1)}{4} \cdot (u_\infty - u_e) + \frac{(c'_\infty + c'_e)}{2} \qquad (86)$$

where $\infty$ and $e$ denote freestream and extrapolated values, respectively. Furthermore, the velocity $v$ and entropy $S$ are specified as freestream values at the inflow, while at the outflow, they are extrapolated from the interior of the computational domain.

From this information at the boundaries, the density and pressure can be computed because,

$$\frac{p}{\rho^\gamma} = \text{function of entropy and } c' = (\gamma \cdot p / \rho)^{1/2}$$

and the entropy, as well as the sonic speed $c'$, are known. The same analysis leading from equation (76) to equation (86) is followed for the upper and lower far-field boundaries, where the derivatives $\partial / \partial x$ are neglected and the velocities $u$ and $v$ are interchanged. This analysis gives the latest updated values at the first 'ghost' cell immediately outside the computational domain. In order to obtain values at the second 'ghost' cell, second-order extrapolation is carried out as shown in equation (42).

Non-reflecting boundary conditions are also a method followed for Euler solvers. In Ref. (24), one such non-reflecting procedure is,

$$\frac{\partial}{\partial t}(p - \rho.u.c') + a \cdot (p - p_\infty) = 0 \qquad (87)$$

where $a = 1 / 8$, an empirical constant. This procedure drives the outflow pressure towards its freestream value. In Ref. (32), Hedstrom proposes a theorem for obtaining non-reflecting boundary conditions as,

$$b_k \cdot \frac{\partial w'}{\partial t} = 0 \qquad\qquad (88)$$

where $b_k$ is an eigenvector corresponding to incoming positive eigenvalues at an inflow and $w'$ denotes the various primitive variables of the Euler equations. In equation (88), for a total of $n$ eigenvalues, with $m$ outgoing characteristics and $k$ incoming characteristics, $m < k < n$. Since the temperature $T$ is taken as one of the primitive variables of the Euler equations, this method appears to guarantee that the enthalpy will remain at its freestream value at the farfield, where $\partial T / \partial t = 0$.

Having justified the choice of the particular numerical procedure, the expressions derived in this chapter are subsequently validated by running the computer code for a variety of test cases. The results obtained from this code are presented in the next chapter.

# CHAPTER 3

# RESULTS AND DISCUSSION

The computer code resulting from the expressions derived in the previous chapter was run for a variety of test cases. The results obtained from this code are discussed in this chapter. All test cases with the exception of the multi-element case (Figs. 13 to 15) are for compressible flow over the NACA 0012 airfoil, which is well documented in the technical literature. The geometry of this symmetric airfoil is given by the following relation for the upper surface (Ref. 33) as,

$$y/c = 0.60 . [ 0.2969 (x/c)^{1/2} - 0.126 (x/c) - 0.3516 (x/c)^2$$
$$+ 0.2843 (x/c)^3 - 0.1015 (x/c)^4 ]$$

where the leading edge is at the origin of the coordinate system.

Fig. 6 shows the results obtained for a freestream Mach Number of 0.5, at zero angle of attack and compares them with the results of Ref. (17) which uses a Cartesian grid and with experimental results from Ref. (33). It is seen that there is good agreement for this subsonic case, run on a 65 x 34 grid, which serves to validate the Euler code.

Fig. 7 compares the results obtained with Ref. (23) which uses a body fitted grid and with Ref. (17), for a freestream Mach Number of 0.8, at zero angle of attack. This is an often used test case for transonic flows. It can be seen that good agreement with the results of Ref. (23) is obtained for the values of the pressure coefficients for the shock peak and the shock foot. However, the shock appears to be one grid point downstream of that of Ref. (23). This may be due to lack of sufficient clustering in the region of the shock. The present work uses a 83 x 34 grid for solving the flow in the upper half-plane of the airfoil. The second order dissipation coefficient $\varepsilon^2$ was locally scaled by a factor of $M^4$ in order to obtain the correct pressure at the shock foot, where M is the local Mach Number in a finite volume cell. Hence, the amount of smearing of the shock in Fig. 7 is seen to be equal to that of Ref. (23). It is interesting to compare the results of Ref. (17)

where the shock peak is one point upstream of Ref. (23). Also, the values of the pressure coefficients for the shock peak and the shock foot in Ref. (17) do not compare favorably with the corresponding results of the present work or with Ref. (23). A comparison of the experimental results of Ref. (33) with the inviscid calculations of Refs. (17), (23) and the present work, shows the effect of the boundary layer on the position of the shock (shifted upstream by 10 % chord).

Convergence upto m significant digits is achieved if the maximum relative error, $\varepsilon$ is less than $5 \cdot 10^{-m}$. Usually this maximum error occurs at the far-field boundaries, where freestream flow prevails, i.e. $\rho_\infty = 1$. The quantity $\partial \rho / \partial t$ is monitored as a measure of convergence and the residue or relative error is denoted as the largest value of $\varepsilon = |\rho^{n+1} - \rho^n / \rho^{n+1}|$ in the entire grid. The calculations were stopped after convergence to the order of $10^{-3}$ was achieved. At this point, the flow picture appears to be fully formed. This is shown in Fig. 8, which describes the convergence history for both subsonic and transonic runs of the code developed in this thesis.

The convergence rates could not be compared with similar Cartesian grid results, as Ref. (17) does not make any mention of this. However, the convergence may be improved by increasing the values of the dissipation coefficients. A Courant Number of 2.0 was used for all calculations. If a local time step is used for convergence acceleration, then the Courant Number is only 1 and the convergence rate can be usefully compared with only that fixed time step which uses a Courant Number of 1.0. In this case, the four-step Runge-Kutta scheme becomes redundant and can be replaced by the MacCormack or Lax-Wendroff schemes, which give a Courant Number of 1.0 - in which case, the considerable saving in computer time resulting from evaluating the spatial derivative terms only twice, becomes a dominant factor. Also, the use of a local time step destroys the time accuracy and is worthwhile only in the final steady state, when the residuals may be of the order of machine zero. However, since the results presented in this thesis are time accurate

with residuals of the order of $10^{-3}$ to $10^{-4}$, it is necessary to use a fixed time step.

The next set of test cases are for lifting flows. Fig. 9 shows the results obtained for the subcritical test case of a freestream Mach Number of 0.5, at an angle of attack of 3 degrees and compares them with those of Ref. (29) and the experimental results of Ref. (33). It can be seen that the present solution resolves the upper surface pressure peak very well. The pressure coefficient prediction for the lower surface is a little higher than that of Ref. (29), which can be due to lack of sufficient clustering at the leading edge. However, there appears to be an overall reasonable level of agreement. This solution used a 65 x 64 grid for the whole airfoil and convergence to the order of $10^{-4}$, was reached in 73 minutes of CPU time on a VAX 8650 computer.

One important feature of the solutions for the lifting test cases is that no Kutta condition was prescribed, yet the correct pressure coefficients are obtained. This was first observed in Refs. (27) and (34), where similar Euler solvers are described. This can be physically valid, if it is considered that the starting.vortex set up at the start of lift, causes a circulation to be established around the airfoil. Thus, circulation is obtained in the absence of vorticity. The Kutta condition requires that for flow past a two-dimensional airfoil, the streamline leaving the trailing edge must bisect the trailing edge angle, if the flow on either side is isentropic. Also, there must be no jump in pressures across this dividing streamline. Obviously this can be accomplished since there is a sharp trailing edge for the NACA 0012 airfoil. Therefore, it can be said that there is a tacit implementation of the Kutta condition at the trailing edge of the airfoil, which comes about by the averaging of the cell-centered primitive variables to evaluate fluxes at the faces of neighbouring.cells.

Fig. 10 compares the results obtained for the supercritical lifting test case of a freestream Mach Number of 0.8, at an angle of attack of $0.37^{\circ}$, with those of Ref. (27). The upper surface pressure distribution shows good agreement regarding strength and location of the shock. The lower surface shock peak is shifted downstream by one grid

42

point as compared to that of Ref. (27). This may be due to the extra grid stretching employed away from the airfoil, which is necessary for convergence of transonic flows. However, the shock strength on the lower surface is correctly predicted. The amount of smearing of both upper and lower surface shocks is the same as in Ref. (27). In Fig. 10, the trailing edge pressure is less than that of Ref. (27), because of lack of adequate grid clustering over there.

In rotational flow, that is transonic flow with different shocks over the upper and lower surfaces of the airfoil, the total pressure behind the shock on the upper surface is less than that on the corresponding point on the lower surface. This forces a difference in the flow velocities causing the inviscid flow to leave at the sharp trailing edge. This 'inviscid separation' kind of behaviour occurs because if the flow along the upper surface (being faster than the flow along the lower surface) of the airfoil, were to expand to infinite values around the trailing edge, then there would have to be a shock at this trailing edge. This would mean a difference in velocities between the upper and lower finite volume cells - which is cancelled out due to the sharp trailing edge. In this case, finite and equal velocities in the upper and lower trailing edge cells is the relevant Kutta condition. This is implicitly satisfied in the present work, as a stable solution. Hence, it is possible to predict with reasonable accuracy, the solutions for both subsonic and transonic lifting test cases .

The third and last objective of this thesis is to compute the flow around multi-element configurations. As a first step towards this goal, the flow over a biplane configuration was computed (see Fig. 11). The two NACA 0012 airfoils are about one chord apart. Calculations were carried out for the upper half of this configuration, that is equivalent to an airfoil hovering about half a chord from the ground or symmetry line. Fig. 12 shows the results for this biplane configuration at a freestream Mach Number of 0.5 and at zero angle of attack. It is seen that the results compare quite well with those of Ref. (17). The upper surface profile does not show any departure from that for an isolated airfoil, while

43

the lower surface profile shows the 'ground effects' on a hovering airfoil.

The final test case is subsonic lifting flow at a freestream Mach Number of 0.5 and at zero angle of attack, over a Karman-Trefftz airfoil with a trailing edge flap and a flap deflection of 10 degrees, as shown in Fig. 13. An exact solution for incompressible flows for the configuration of Fig. 13, was obtained by Williams in Ref. (35). A grid of size 194 x 64 was used for this test case. Two blocks were generated separately for the main airfoil and for the flap and were spliced together at the region of overlap. Since the same grid size is maintained for both blocks, there is no loss of continuity for the transformation metrics $\partial \xi / \partial x$ and $\partial \eta / \partial y$. This testifies to the ease in applying Cartesian grids to multi-element blocks.

Figs. 14 and 15 compare the results obtained in the present work with that of Ref. (17). Fig. 14 compares the results for the main airfoil. Though the results do not agree well, it is seen that there is general agreement. The principal discrepancy is at the leading edge, as a consequence of the lack of adequate grid clustering over there. The pressure coefficient prediction in Ref. (17) is also not very accurate and the value at the leading edge is also much lower than the desired value. Fig. 15 compares the results for the trailing edge flap. It is seen that the pressure coefficient prediction for the lower surface agrees quite well with the desired values, while that for the upper surface does not. This can be due to the fact that some points on the leading edge were not captured by the spline fit used in the present work. On the whole, it appears to satisfy the third objective of this thesis - to demonstrate the application of Cartesian grids to multi-element airfoils.

# CONCLUSIONS

An Euler code has been developed for computing steady, two-dimensional inviscid flows over airfoils, by discretizing the flow domain into finite volumes on a Cartesian grid and the solution is marched in time, using a fourth order Runge-Kutta time-stepping scheme. The results obtained cover subsonic and transonic flows for standard test cases on a NACA 0012 airfoil, as well as a multi-element case.

Hence, the following observations about the results can be made as :

(1) They are in agreement (within an error margin of about 3 %, or one grid point - regarding the location of the inviscid shock) with Jameson's Euler code.

(2) They compare qualitatively with experimental results.

(3) The code can be used for multi-element airfoils as well.

As analyzed in Chapter 2 of this thesis, the Runge-Kutta scheme can be substituted for, by other alternative schemes like the MacCormack method, etc. Therefore, this code can handle a variety of applications.

## Suggestions for future work :

Future work should be in the direction of three-dimensional extensions to this code, multi-grid techniques, convergence acceleration techniques like 'enthalpy damping' and 'residual-averaging' methods, techniques for improving the resolution of shock-waves like 'total variation diminishing' methods, application of above techniques for study of viscous-inviscid interactions and finally solutions for the complete Navier-Stokes equations themselves, in primitive variable form.

# REFERENCES

(1)    Steinhoff, J. and Jameson, A., "Multiple Solutions of the Transonic Potential Flow Equation," AIAA Paper 81-1019, 1981.

(2)    Salas, M.D., Jameson, A. and Melnik, R.E., "A Comparative Study of the Nonuniqueness Problem of the Potential Equation," AIAA Paper 83-1888, 1983.

(3)    Hafez, M. and Lovell, D., "Entropy and Vorticity Corrections for Transonic Flows," AIAA Paper 83-1926, 1983.

(4)    Habashi, W.G., Hafez, M.M. and Kotiuga, P.L., "Finite Element Methods for Internal Flow Calculations," AIAA Paper 83-1404, 1983.

(5)    Hafez, M. and Lovell, D., "Numerical Solution of Transonic Stream Function Equation," AIAA Journal, Vol. 21, No. 3, March 1983, pp. 327-335.

(6)    Habashi, W.G. and Hafez, M.M, "Finite Element Stream Function Solutions for Transonic Turbomachinery Flows," AIAA Paper 82-1268, 1982.

(7)    Atkins, H.L. and Hassan, H.A., "A New Stream Function Formulation for the Steady Euler Equations," AIAA Journal, Vol. 23, No. 5, May 1985, pp. 701-706.

(8)    Magnus, R. and Yoshihara, H., "Inviscid Transonic Flow over Airfoils," AIAA Journal, Vol. 8, No. 12, December 1970, pp. 2157-2162.

(9)    Beam, R.M. and Warming, R.F., "An Implicit Finite-Difference Algorithm for Hyperbolic Systems in Conservation Law Form, Journal of Computational Physics, Vol. 22, pp. 87-110 (1976).

(10)   Jameson, A., Schmidt, W. and Turkel, E., "Numerical Solutions of the Euler Equations by Finite Volume Methods using Runge-Kutta Time-Stepping Schemes," AIAA Paper 81-1259, 1981.

(11)   Dick, E., "The Calculation of Steady Transonic Flow by Euler Equations with

Relaxation Methods," in <u>Computational Methods for Turbulent, Transonic and Viscous Flows</u> - ed. J.A. Essers, Hemisphere Publishing Corporation 1983, pp. 291-350.

(12)    Johnson, G.M., "Accelerated Solution of the Steady Euler Equations," in <u>Advances in Computational Transonics</u> - ed. W.G. Habashi, Pineridge Press (U.K.) 1984, pp. 473-501.

(13)    Carey, G.F., "An Analysis of Stability and Oscillations in Convection-Diffusion Computations," in <u>Finite Element Methods for Convection Dominated Flows,</u> AMD - Vol. 34 - ed. T.J.R. Hughes, ASME 1979, pp. 63-71.

(14)    Steger, J.L. and Warming, R.F., "Flux Vector Splitting of the Inviscid GasDynamic Equations with Application to Finite-Difference Methods," <u>Journal of Computational Physics,</u> Vol. 40, pp. 263-293 (1981).

(15)    Thompson, J.F., Warsi, Z.U.A. and Mastin, C.W., "Boundary Fitted Coordinate Systems for Numerical Solution of Partial Differential Equations - A Review," <u>Journal of Computational Physics,</u> Vol. 47, pp. 1-108 (1982).

(16)    Wedan, B. and South, J.C., Jr., "A Method for Solving the Transonic Full-Potential Equation for General Configurations," AIAA Paper 83-1889, 1983.

(17)    Clarke, D.K., Salas, M.D. and Hassan, H.A., "Euler Calculations for Multi-Element Airfoils using Cartesian Grids," <u>AIAA Journal,</u> Vol. 24, No. 3, March 1986, pp. 353-358.

(18)    Habashi, W.G. and Grumbir, R., "Solution of the Potential and Euler Equations on Cartesian grids," report submitted to Department of Supplies and Services, Canada, for Contract # OST 85-00089 (1986).

(19)    Jones, D.J., "Private Communication," National Research Council, Ottawa (1986).

(20)     Gaffney, R.L., Jr., Salas, M.D. and Hassan, H.A., "Euler Calculations for Wings Using Cartesian Grids," AIAA Paper 87-0356, 1987.

(21)     Anderson, D.A., Tannehill, J.C. and Pletcher, R.H., "Computational Fluid Dynamics and Heat Transfer," Hemisphere Publishing Corporation 1984, pp. 1-599.

(22)     Pulliam, T.H., "Artificial Dissipation Models for the Euler Equations," <u>AIAA Journal</u> Vol. 24, No. 12, December 1986, pp. 1931-1940.

(23)     Pulliam, T.H., "Implicit Finite Difference Methods for the Euler Equations," in <u>Advances in Computational Transonics</u> - ed. W.G. Habashi, Pineridge Press (U.K.) 1984, pp. 503-542.

(24)     Jameson, A., Schmidt, W. and Turkel, E., "Numerical Solutions of the Euler Equations by Finite Volume Methods using Runge-Kutta Time-Stepping Schemes," AIAA Paper 81-1259, 1981.

(25)     Jameson, A., "Transonic Airfoil Calculations Using the Euler Equations," in <u>Numerical Methods in Aeronautical Fluid Dynamics</u> - ed. P.L. Roe, Academic Press, 1982, pp. 289-308.

(26)     Schmidt, W. and Jameson, A., "Euler Solvers as an Analysis Tool for Aircraft Aerodynamics," in <u>Advances in Computational Transonics</u> - ed. W.G. Habashi, Pineridge Press (U.K.) 1984, pp. 371-404.

(27)     Schmidt, W., Jameson, A. and Whitfield, D., "Finite-Volume Solutions to the Euler Equations in Transonic Flow," <u>Journal of Aircraft</u>, Vol. 20, No. 2, February 1983, pp. 127-133.

(28)     Jameson, A., "Numerical Solution of the Euler Equations for Compressible Inviscid Fluids," in <u>Numerical Methods for the Euler Equations of Fluid Dynamics</u> - ed. F. Angrand et al, SIAM 1985, pp. 199-231.

(29)     Jameson, A. and Yoon, S., "Multigrid Solution of the Euler Equations using

Implicit Schemes," <u>AIAA Journal</u>, Vol. 24, No. 11, November 1986, pp. 1737-1743.

(30)   Turkel. E, "Acceleration to a Steady State for the Euler Equations," in <u>Numerical Methods for the Euler Equations of Fluid Dynamics</u> - ed. F. Angrand et al, SIAM 1985, pp. 199-231.

(31)   Salas, M.D. and Thomas, J.L., "Far-Field Boundary Conditions for Transonic Lifting Solutions to the Euler Equations," <u>AIAA Journal</u>, Vol. 24, No. 7, July 1986, pp. 1070-1080.

(32)   Hedstrom, G.W., "Nonreflecting Boundary Conditions for Nonlinear Hyperbolic Systems," <u>Journal of Computational Physics</u> , Vol. 30, pp. 222-237 (1979).

(33)   Thibert, J.J., Grandjacques, M. and Ohman, L.H., "NACA 0012 Airfoil," in <u>Experimental Data Base for Computer Program Assessment</u>, AGARD Advisory Report No. 138 (1979).

(34)   Rizzi, A., "Mesh Influence on Vortex Shedding in Inviscid Flow Computations," in <u>Recent Contributions to Fluid Mechanics</u> - ed. W. Haase, Springer Verlag 1982, pp. 213-221.

(35)   Williams, B.R., "An Exact Test Case for the Plane Potential Flow about Two Adjacent Lifting Airfoils," Aeronautical Research Council, R&M 3717, 1973.

# FIGURES
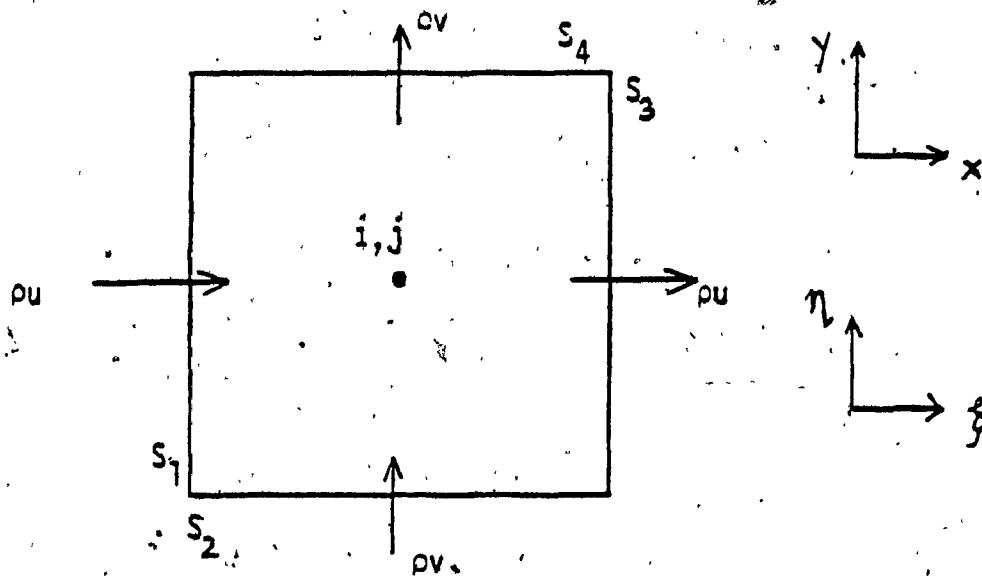
Fig. 1   Typical flux cell
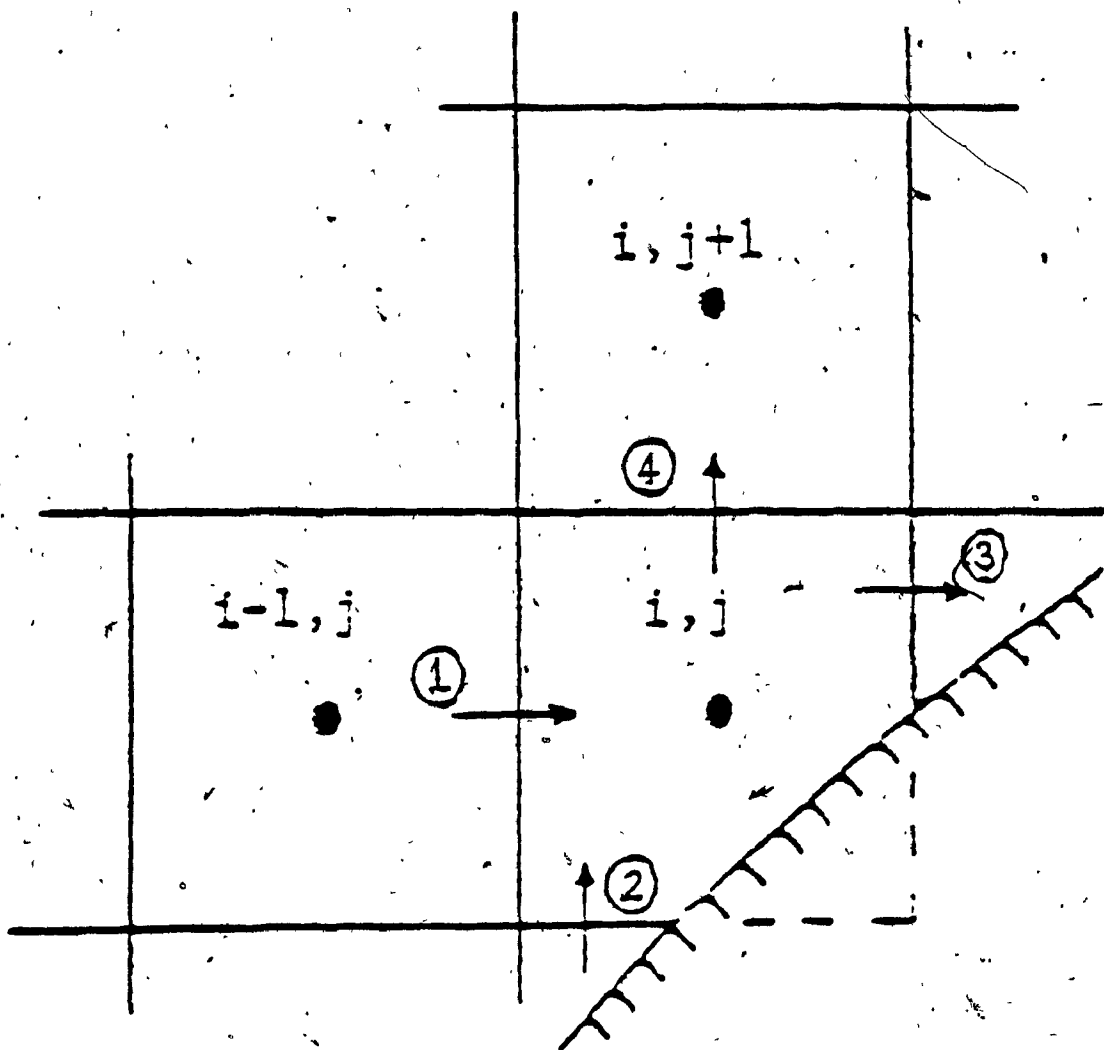
Fig. 2  Boundary cell
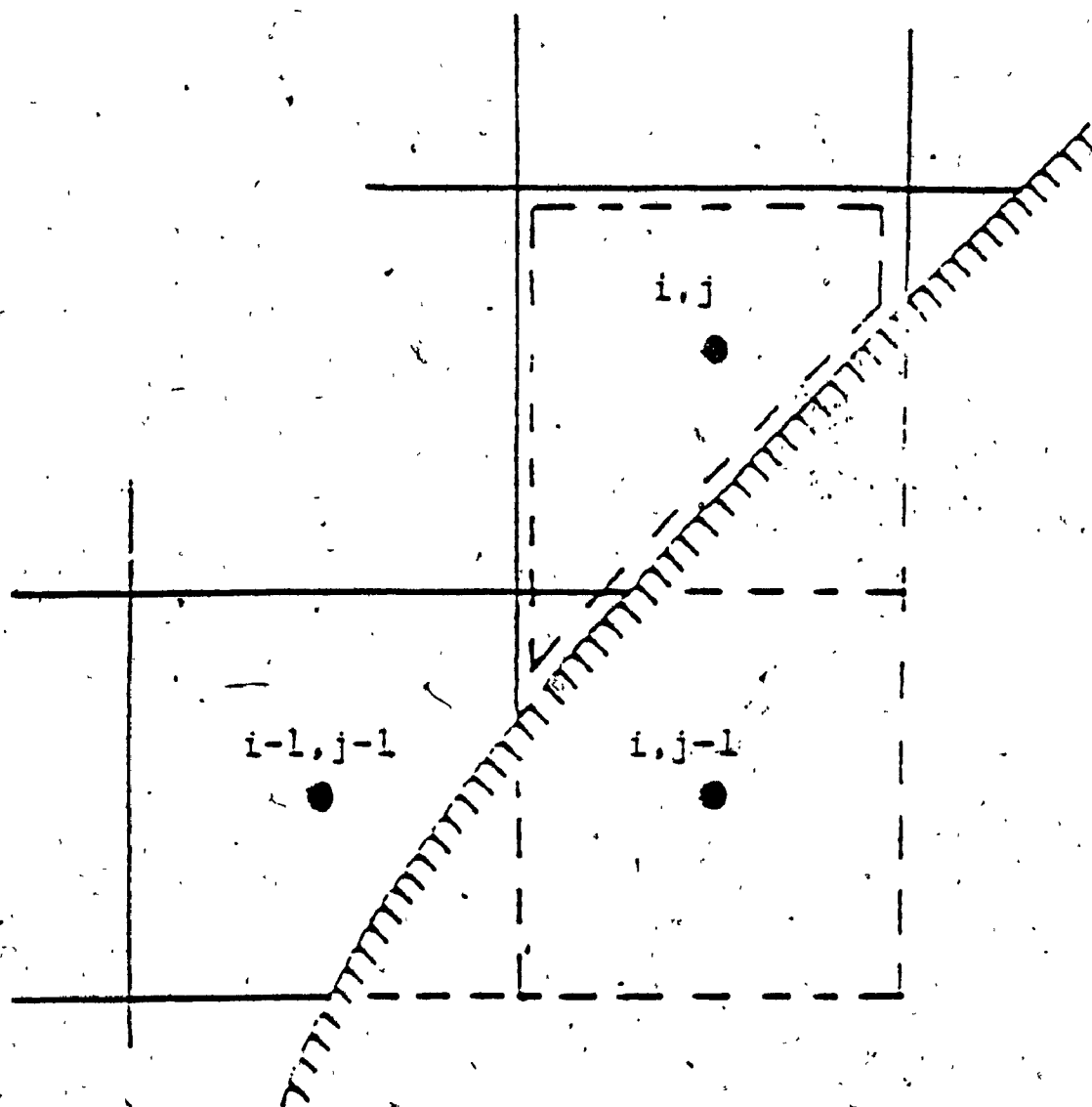
Fig. 3 . Addition of small cells
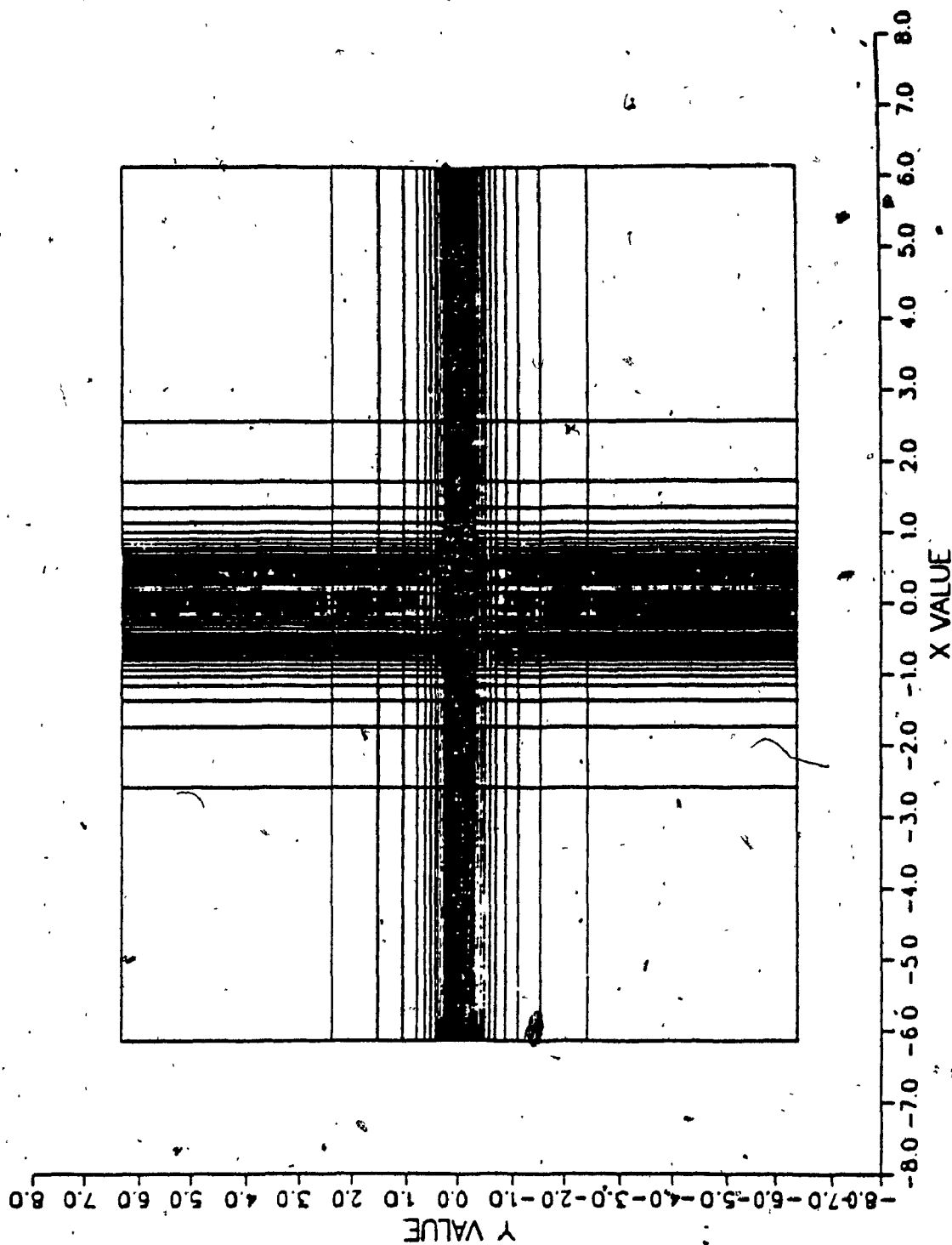
Fig. 4    Plot of grid (61 x 61)
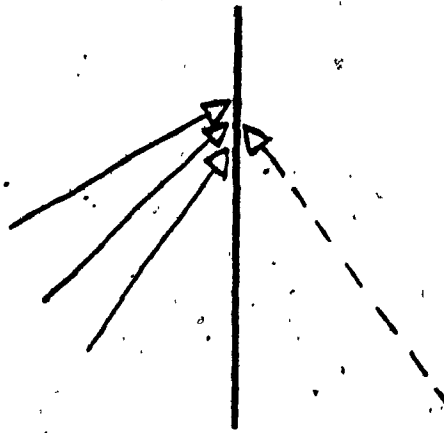
Fig. 5a   Inflow boundary characteristics
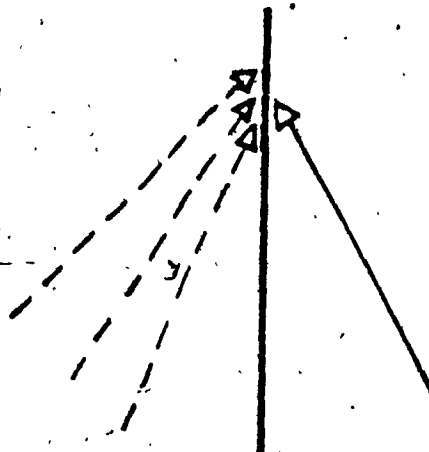


Fig. 5b   Outflow boundary characteristics
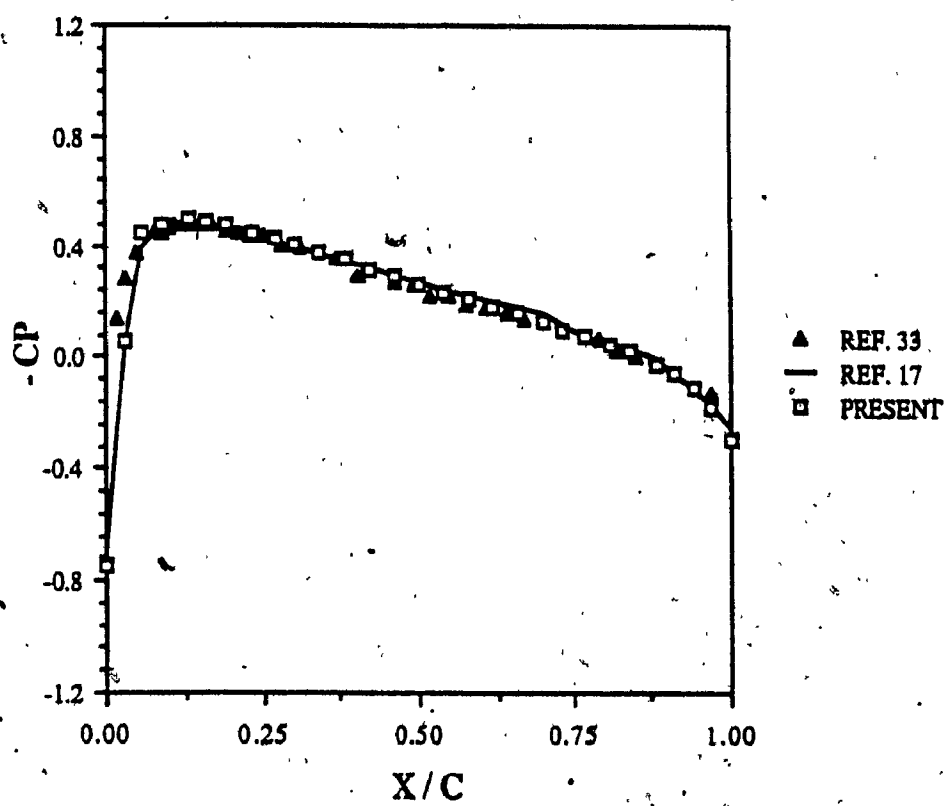
Fig. 6 Solution of a subsonic flow
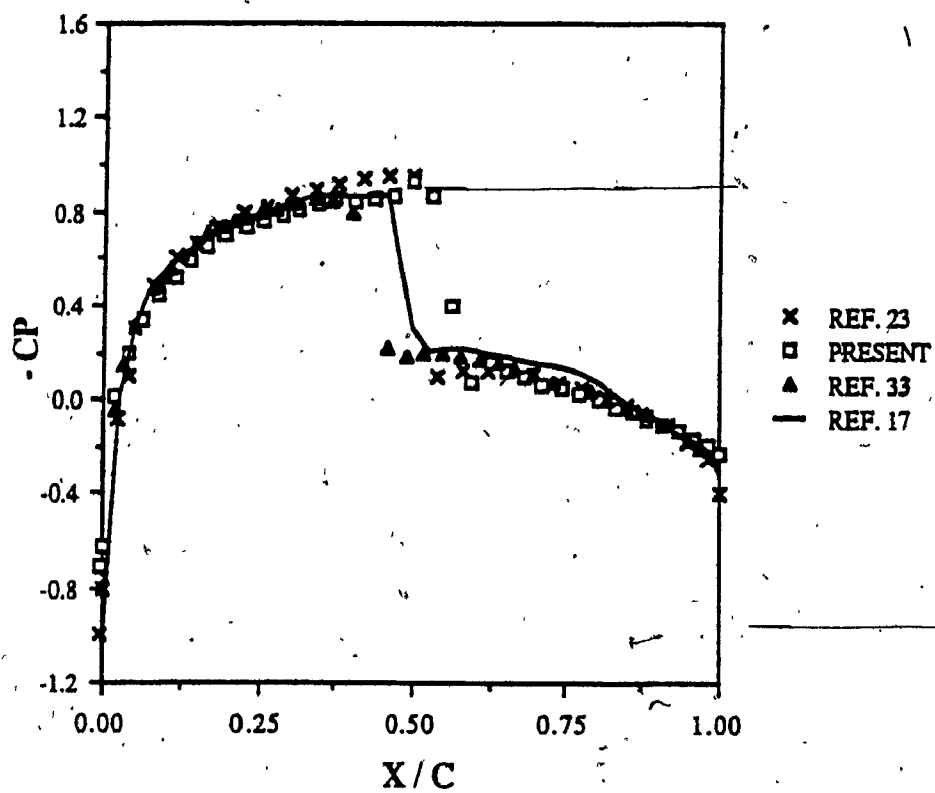
$( M_\infty = 0.5, \alpha = 0^\circ )$

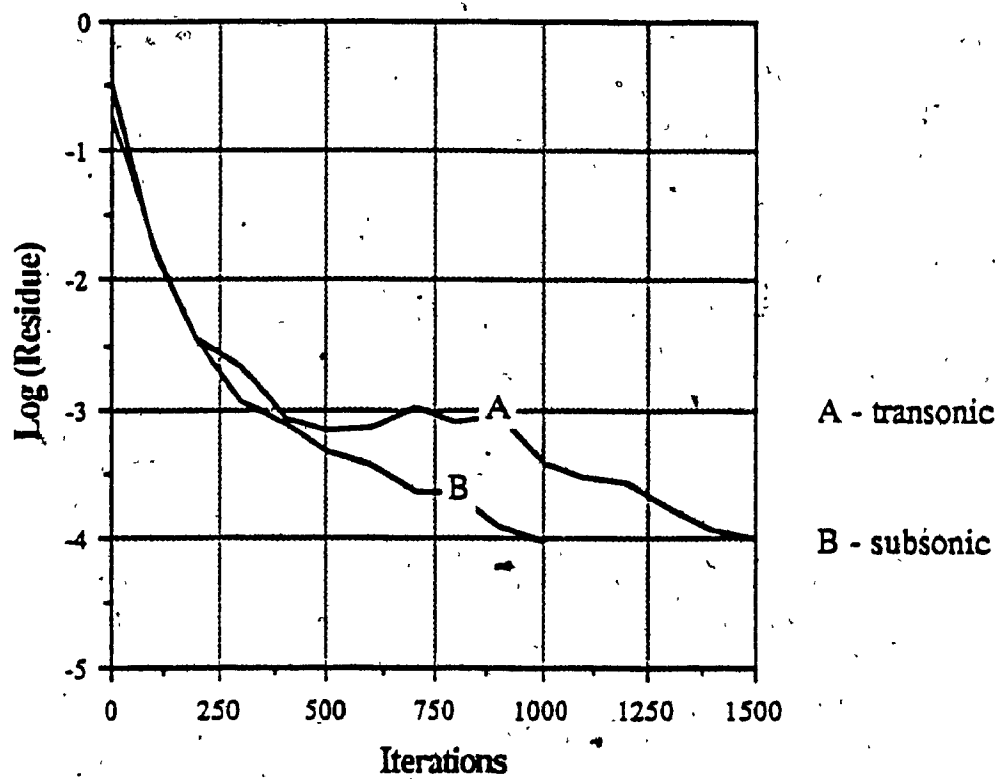Fig. 7 Solution of a transonic flow

$( M_\infty = 0.8, \alpha = 0^\circ )$
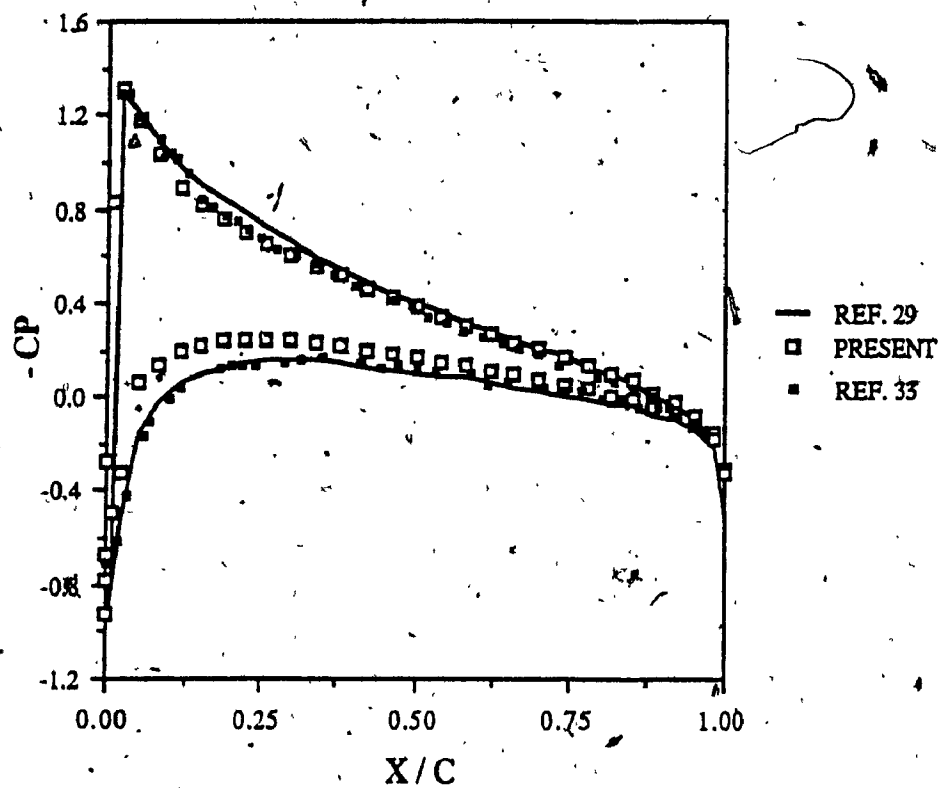
Fig. 8   Convergence Histories

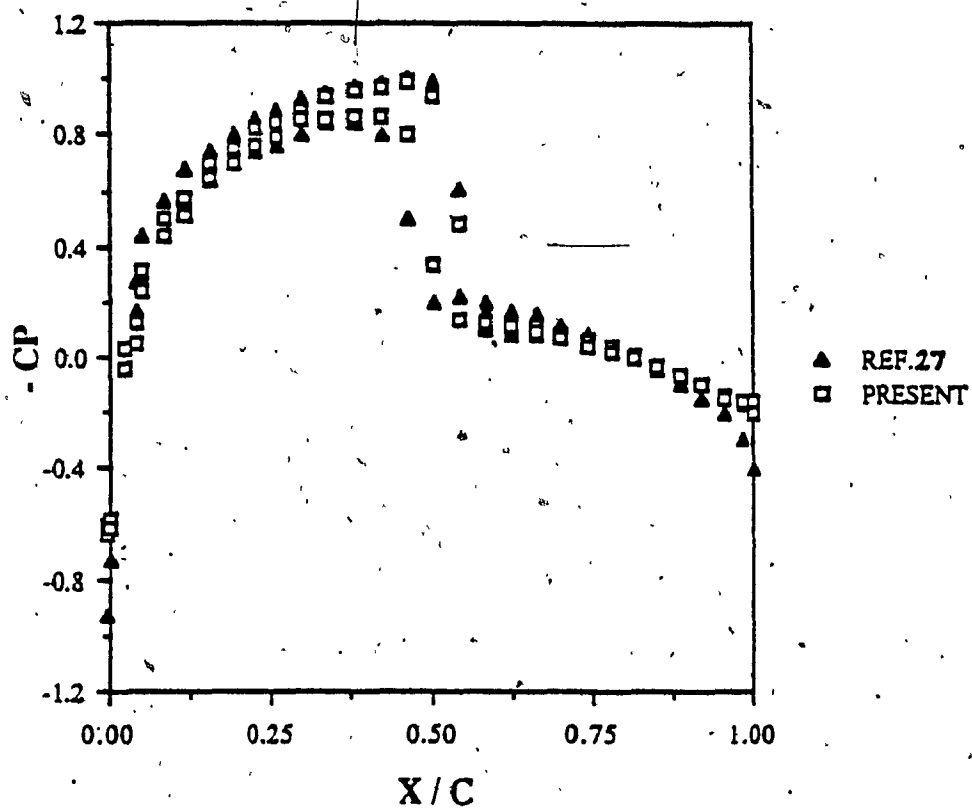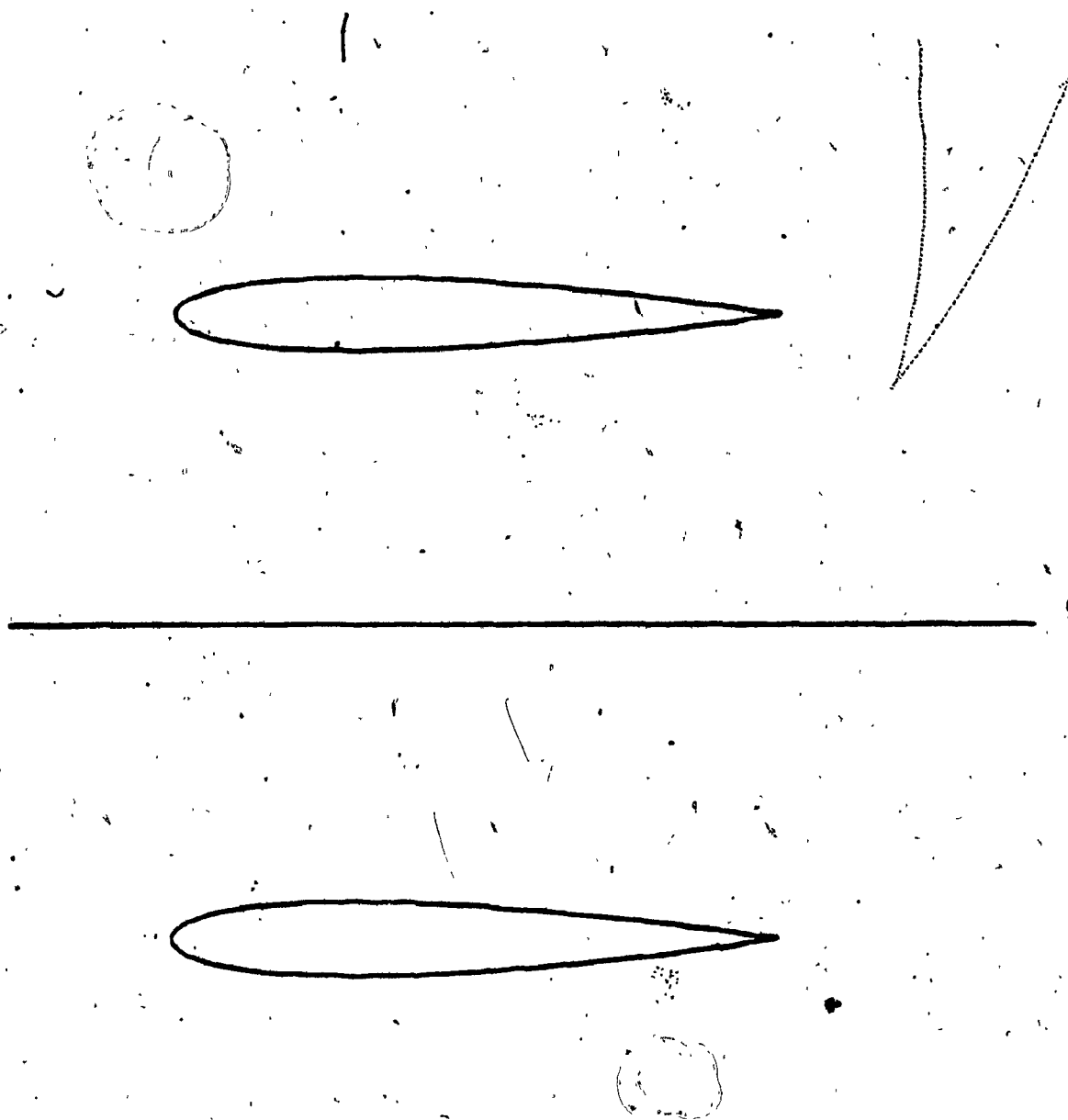Fig. 9    Solution of a subsonic lifting flow

$( M_{\infty} = 0.5, \alpha = 3^{\circ} )$

Fig. 10    Solution of a transonic lifting flow

$(M_\infty = 0.8, \alpha = 0.37°)$

59

Fig. 11   Biplane configuration
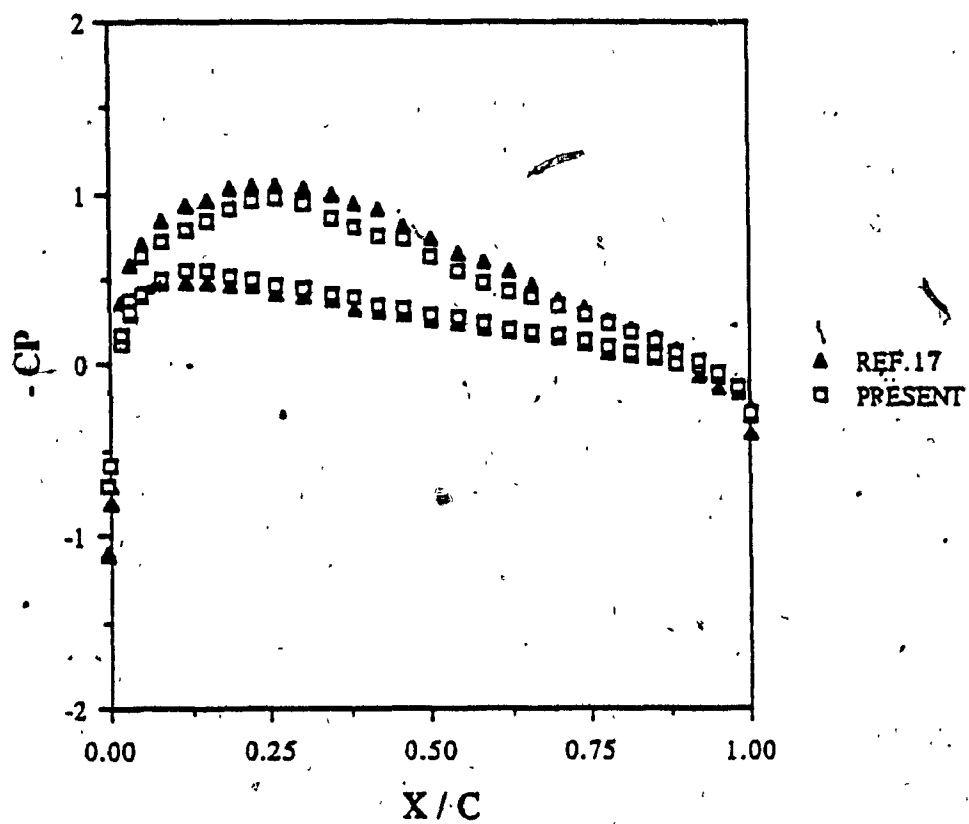
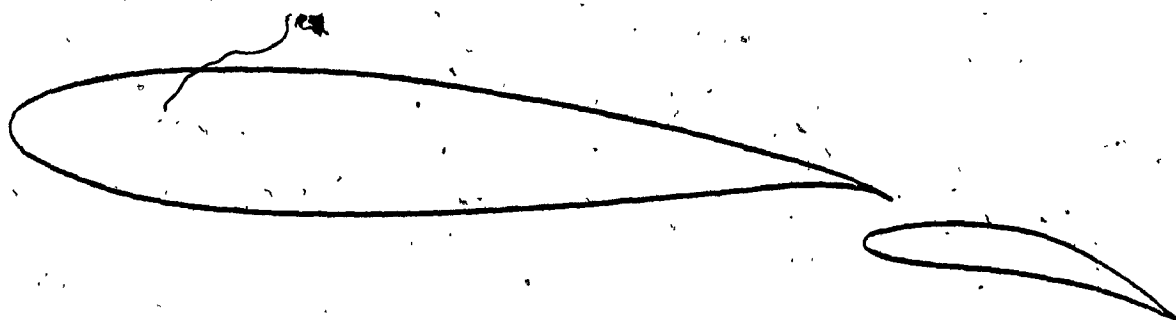Fig. 12    Subsonic results for Biplane

$(M_\infty = 0.5, \alpha = 0°)$

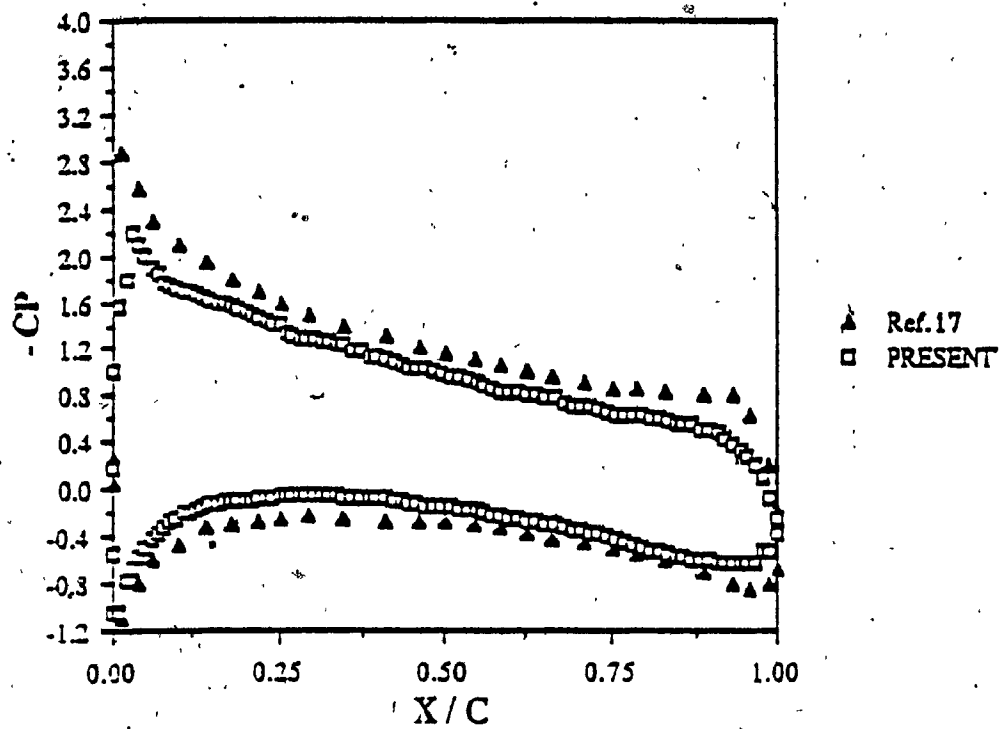Fig. 13   Multi-element Configuration  ($M_\infty = 0.5, \alpha = 0^\circ$)

62

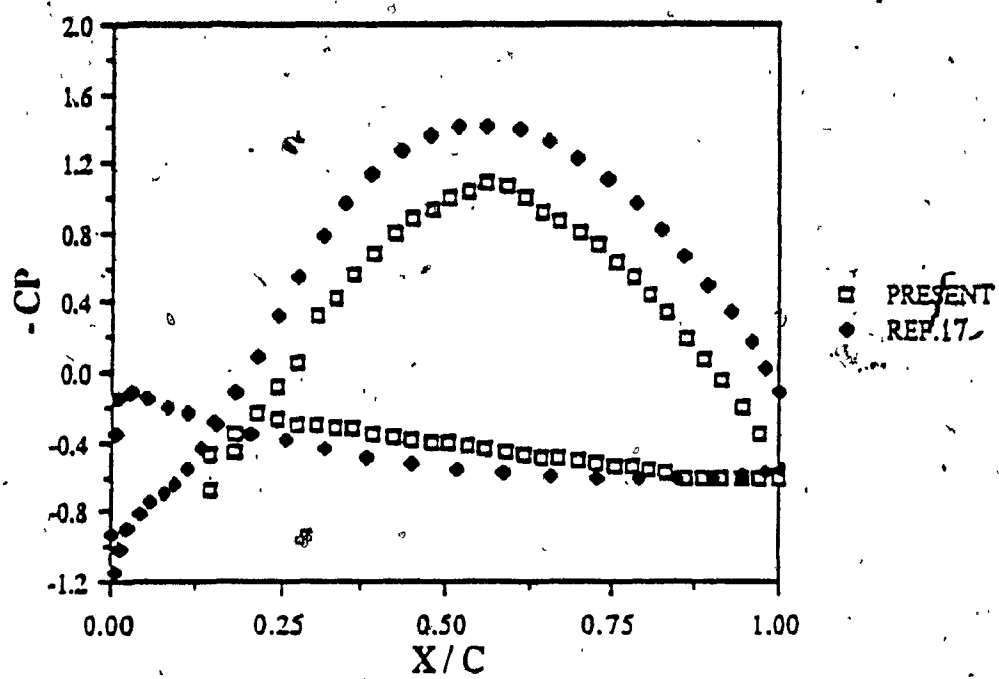Fig. 14    Subsonic results for main airfoil of Fig. 13

Fig. 15 . Subsonic results for trailing edge flap of Fig. 13 , at $\alpha = 10^\circ$